

Toward the perfect membrane material for environmental x-ray photoelectron spectroscopy

Paul Leidinger^{1,2} , Jürgen Kraus^{1,2}, Tim Kratky^{1,2} , Patrick Zeller^{1,4},
Tevfik Onur Menteş³, Francesca Genuzio³, Andrea Locatelli³ and Sebastian Günther^{1,2,*} 

¹ Technical University of Munich (TUM), Chemistry Department, Physical Chemistry with Focus on Catalysis, Lichtenbergstr 4, D-85748 Garching, Germany

² Catalysis Research Center, Ernst-Otto-Fischer-Straße 1, D-85748 Garching, Germany

³ Elettra, Sincrotrone Trieste S.C.p.A., Area Science Park, Basovizza, I-34149 Trieste, Italy

E-mail: sebastian.guenther@tum.de

Received 14 December 2020, revised 29 January 2021

Accepted for publication 17 February 2021

Published 15 March 2021



CrossMark

Abstract

We outline our achievements in developing electron transparent, leak-tight membranes required for environmental photoelectron spectroscopy (PES). We discuss the mechanical constraints limiting the achievable membrane size and review the development of growth protocols for the chemical vapor deposition (CVD) of single-crystalline graphene on highly (111) textured Cu foils serving as membrane material. During CVD growth, Cu tends to develop a mesoscopic staircase morphology consisting of alternating inclined surface planes, irrespective of whether the covering graphene film or the substrate are single-crystalline. This morphology remains imprinted even when converting the film into freestanding graphene, which affects its mechanical properties. Determining the number of carbon layers in freestanding graphene, we show that membranes reported to suspend over distances larger than 20 μm most likely consist of few-layer graphene. The Raman band signature often used to confirm monolayer graphene rather relates to graphene with turbostratic stacking. The vertical corrugation of freestanding graphene was shown to be almost absent for tri- and four-layer-thick graphene but substantial for bilayer and especially for monolayer graphene. The corrugation is reduced when mechanically straining the freestanding graphene through thermal expansion of the supporting frame, especially flattening membrane areas with imprinted staircase morphology. The electron signal attenuation through supported and freestanding graphene was determined as a function of the electron kinetic energy, verifying that large-area graphene-based electron windows have sufficient electron transparency required for environmental PES. Meanwhile, we managed to cover 100 μm -sized single holes by few-layer graphene up to a coverage fraction of over

⁴ Current address: Helmholtz-Zentrum Berlin für Materialien und Energie GmbH, BESSY II, Albert-Einstein-Straße 15, 12489 Berlin, Germany and Fritz-Haber-Institut der Max Planck Gesellschaft, Dept. Inorganic Chemistry, Faradayweg 4-6, 14195 Berlin, Germany

* Author to whom correspondence should be addressed.



Original content from this work may be used under the terms of the [Creative Commons Attribution 4.0 licence](https://creativecommons.org/licenses/by/4.0/). Any further distribution of this work must maintain attribution to the author(s) and the title of the work, journal citation and DOI.

99.9998%, as deduced when applying 10 mbar air on one side of the sealing membrane without detecting any measurable pressure increase on its ultrahigh vacuum side. The reported achievements will pave the way toward the development of laboratory-based environmental PES.

Supplementary material for this article is available [online](#)

Keywords: graphene, chemical vapor deposition, electron transparency, membranes, environmental cell, x-ray photoelectron spectroscopy, freestanding graphene

(Some figures may appear in colour only in the online journal)

1. Introduction

After the discovery of graphene as a two-dimensional (2D) solid consisting of a single carbon layer with a honeycomb lattice, the extraordinary mechanical and electronic properties of this intriguing material induced extensive research activity [1–3]. Besides the importance of graphene regarding its electronic band structure with Berry phase properties [4], the material is outstanding because of its high mechanical stability [5], atomic impermeability [6], chemical inertness and high electronic conductivity and mobility [1]. These properties will lead or have already led to the development of novel devices, such as small pressure sensors [7, 8], transistors [9], thin electrode materials [10, 11], corrosion protection layers [12] or atomically thin, gas-tight [6] or semipermeable [13] membranes.

One of the novel applications is the construction of a gas-tight membrane that is thin enough to be transparent even for electrons with low kinetic energy. Lenard already used very thin Al foils as electron transparent windows for highly energetic electrons generated in a cathode ray tube, a work which was awarded the Nobel Prize in Physics in 1905 [14]. The concept of electron transparent windows capable of sealing a specimen in a vacuum-incompatible environment was applied in electron microscopy shortly after its invention in the 1930s (see, e.g. [15, 16]). Meanwhile, electron microscopy of vacuum-incompatible samples is called environmental transmission- [17] or environmental scanning electron microscopy [18, 19] and microchips with cavities sealed by several nm thick membranes are commercially available as environmental cells [20, 21]. Nevertheless, these membranes are non-transparent for slow electrons. Due to the dramatic increase of inelastic electron scattering in solid matter with decreasing kinetic energy [22, 23], such devices cannot be used for applications such as photoelectron spectroscopy (PES), and in particular x-ray photoelectron spectroscopy (XPS), where photoelectrons with a kinetic energy between 50 and 1500 eV are collected. When using graphene oxide or graphene as an alternative electron transparent window material, these shortcomings are overcome [24, 25]. Before graphene-sealed environmental cells were available, the only alternative approach to so-called ambient pressure XPS made use of differentially pumped electron analyzers, which were operated in a laboratory up to pressures close to the 10 mbar

range [26–28]. When using highly brilliant synchrotron light, the setup can be modified, and pressures well above 10 mbar and recently up to more than 1 bar became possible [29–33].

Meanwhile, the environmental cell approach toward ambient pressure XPS has proven to be a very promising way to allow the characterization of catalytic surfaces inside a high-pressure or liquid environment. In current environmental cell-based ambient pressure setups the hole diameter covered by freestanding graphene is greatly reduced with respect to the nominally limiting values, as will be separately discussed further below. Typically, single holes or hole arrays of 1–4 μm in diameter maximum are sealed [34–37]. Apart from electron windows, the investigation of liquid droplets enclosed between two membranes in contact with each other is also reported in the literature [38, 39]. A potential leakage due to local failure of the double-sided membrane does not spoil the base pressure of the surrounding vacuum chamber due to the small amount of material that is released into the vacuum. The benefit of the approach is that local membrane failure reduces the amount of droplets but does not prevent study of the remaining ones.

Environmental cells with a single hole as the electron window have been successfully assembled with few-layer graphene or graphene oxide as the sealing membrane material, and proof-of-principle XPS of statically enclosed liquids has been performed [24, 25, 40, 41]. A pressure relief membrane on the backside of the cell reduces the pressure difference during the pumping down of the system. The single-hole structures were also extended to cells with sealed arrays of micro cavities [37, 42]. In such setups, the advantage is preserved that local membrane rupture does not lead to catastrophic damage and venting of the vacuum system, and allows investigation of the remaining sealed cavities under ambient conditions. However, in both geometries, the filling medium of the cavities cannot be exchanged. This disadvantage becomes important, especially when exposing liquids to highly brilliant x-ray (or electron) irradiating beams. For example, radiolysis of water was observed, leading to gas accumulation and bubble formation underneath the membrane, which finally breaks upon prolonged irradiation [25].

Beam damage effects are reduced when exchanging the dense medium inside the environmental cell during operation, which also allows *in situ* flow-type reactor studies to be performed. Therefore, cells have been developed that make use of electron windows based on interconnected arrays of holes

covered by graphene. Typically, the support structure hosting the holes is made out of a thin silicon nitride membrane, which is transparent for the irradiating x-rays [34, 35, 43, 44] so that the photoelectron emission yield is limited by the electron transparency of the window only. The latter quantity scales with the hole-to-support-area ratio of the array, which is small due to the small hole size (typically $<1 \mu\text{m}$) and the large hole separation distance ($>5 \mu\text{m}$). The entire array is also limited in size to minimize the leakage rate through the operating membrane and the potential area where the graphene sealing might break. As a result, the chosen thickness of the sealing membrane is a compromise of the increased sealing capability at the cost of an exponentially decreasing electron transparency. In order to compensate for the low photoelectron emission through such electron windows, brilliant x-rays provided by synchrotron light facilities are used. All studies are typically performed at differentially pumped electron spectrometers because of the potential risk of membrane rupture and the overall limited leak tightness of the electron window. Nevertheless, the use of microfluidic cells covered by an electron window with graphene-sealed hole arrays might pave the way to setups that do not require differential pumping at all [42].

Radical formation during x-ray irradiation was shown to significantly affect the chemical system even when being characterized in SiN-sealed environmental cells using x-ray absorption spectroscopy in synchrotron studies [45]. Since a decreased photon density reduces the observed beam damage, an enlarged electron transparency of the electron window would allow photoelectron spectra with equal signal-to-noise ratio to be acquired at a reduced photon intensity. Enlarging the size of the electron window also reduces beam damage as the irradiating photons can be distributed over a larger area. Thus, the development of electron windows with high electron transparency over the maximum achievable area is the technical goal of the environmental cell approach towards ambient pressure XPS. One way to meet this target is to produce large-area electron windows at the cost of leak tightness, i.e. it was possible to develop an electron transparent 1 mm^2 -sized Pt working electrode of an environmental electrochemical cell that could be investigated by *in situ* ambient pressure XPS. The catalytic Pt particles deposited on the backside of the graphene film mechanically stabilized the electrode on top of a proton exchange membrane. The leakage through the graphene sealing led to a background pressure of about 0.1 mbar so that the studies required differential pumping of the electron analyzer [46].

So far, all state-of-the-art environmental cell-based ambient pressure XPS experiments have used differentially pumped electron analyzers at synchrotron light facilities with electron transparent graphene membranes that locally cover only μm -sized distances as freestanding graphene. Meanwhile, the synthesis of freestanding graphene over much larger areas has been reported in the literature [47–49], indicating that nominally much larger, leak-tight electron windows might become possible. Thus, one can imagine achieving the ultimate goal of turning ambient pressure XPS into a

laboratory-based technique. The feasibility of this ultimate goal is the topic of our review.

After a short paragraph reporting on the experimental details in section 2, we discuss the nominal mechanical stability limit of monolayer graphene membranes in section 3. Graphene is an extremely mechanically stable material but reaches its properties only if it is of high crystalline quality. We have been working on this topic for more than 9 years, trying to push the crystalline quality so that it fulfills the requirements of the technique. During this time, one of the most promising synthesis routes toward a highly crystalline material has been the chemical vapor deposition (CVD) growth of graphene on Cu. We also follow this synthesis route in our group and review our work in section 4 of the manuscript. In section 5, we outline the experimental techniques on how to transform supported into freestanding graphene, which can be regarded as the next step in the assembly of graphene-based membranes. Here, remarkable results have been reported in the literature [48–54]. With the ability to produce large, freestanding graphene membranes, we can follow their mechanical properties and also turn them into surfaces well ordered on the atomic scale. In section 6, we outline novel experiments by acquiring real and reciprocal space information for freestanding graphene using scanning electron microscopy (SEM), Raman spectroscopy and low-energy electron microscopy (LEEM). Finally, we address the electron transparency and the achievable leak tightness of the assembled window material, which is the topic of sections 7 and 8, showing that we are able to seal $>99.9998\%$ of $100 \mu\text{m}$ diameter holes by a suspended graphene membrane. Our results indicate that the laboratory-based environmental cell approach toward ambient pressure XPS should become possible.

2. Methods

The experimental data shown here were acquired with a variety of laboratory techniques. Optical microscopy images were recorded using an Olympus BH-2 microscope. Raman spectra were measured using a Horiba-Jobin-Yvon HR800 UV spectrometer coupled to a HeNe laser ($\lambda = 632.8 \text{ nm}$). SEM was performed using a Hitachi S-3200 N instrument using a beam energy of 5 keV or 10 keV at an emission current of 70 mA by acquiring the secondary electron emission yield with the help of an Everhart–Thornley detector. Scanning Auger microscopy (SAM) was performed using a Staib Auger electron spectrometer equipped with an EK-5-IK electron gun inside a DESA 100 CMA analyzer (primary energy: 5 kV). Finally, x-ray photoelectron spectra were acquired using a VSW instrument including a non-monochromatic x-ray anode (TA10, VSW) and a hemispherical analyzer (HA100, VSW) with a channeltron multiplier as the electron detector. Sample cleaning and surface layer removal from Cu was performed by Ar^+ ion sputtering at 2 kV using 5.0 quality Ar gas. The LEEM experiments were performed at the Nanospectroscopy beamline of the Elettra synchrotron facility using the

Table 1. Pre-treatment of the Cu foil in the loaded reactor prior to performing the actual CVD process.

Pre-treatment	Synthesis protocol prior to CVD synthesis
A	Temperature increase of the Cu-loaded reactor in: $p(\text{H}_2) = 0.5$ mbar up to 950°C (1223 K) within 40 min, increase to $p(\text{H}_2) = 50$ mbar for 90 min
B	Temperature increase of the Cu-loaded reactor in: $p(\text{H}_2) = 0.5$ mbar up to 950°C (1223 K) within 40 min, exchange reactor atmosphere to: $p(\text{Ar}) = 1$ mbar + $p(\text{O}_2) = 7.5 \times 10^{-6}$ mbar at 950°C for 60 min
C	Temperature increase of the Cu-loaded reactor in: $p(\text{H}_2) = 0.5$ mbar up to 950°C (1223 K) within 40 min, exchange reactor atmosphere to: $p(\text{Ar}) = 1$ mbar + $p(\text{O}_2) = 7.5 \times 10^{-6}$ mbar at 950°C for 30 min, exchange reactor atmosphere to: $p(\text{H}_2) = 100$ mbar at 1050°C for few min

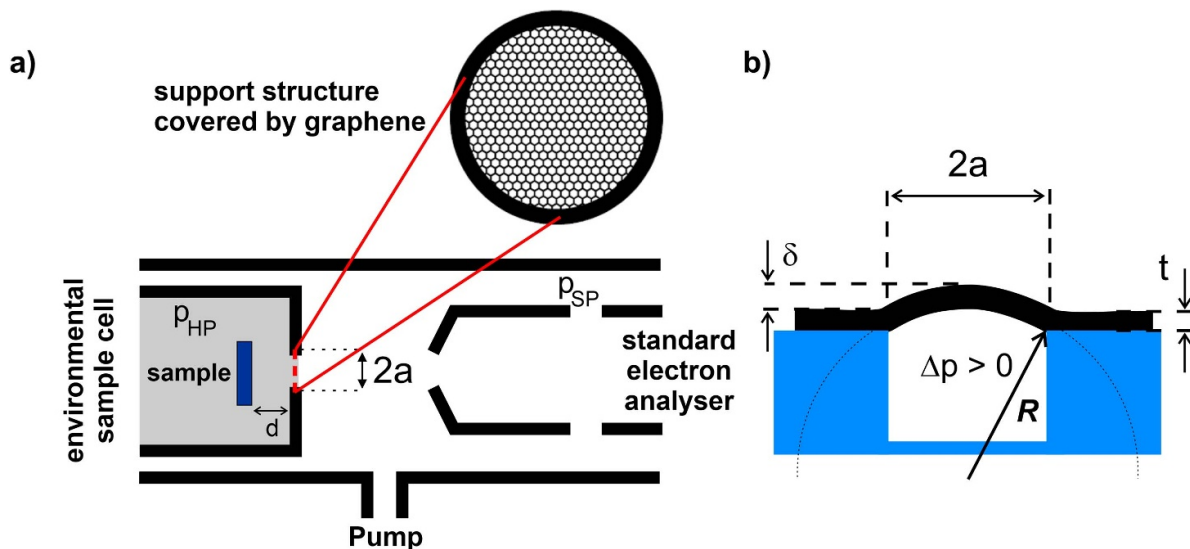


Figure 1. (a) Ultimate goal of x-ray photoelectron spectroscopy (XPS) measurement characterizing a sample at environmental conditions through a graphene membrane-sealed cell. The released photoelectrons can penetrate the ultrathin graphene membrane and turn standard ultrahigh vacuum XPS equipment into an environmental XPS system. The envisioned environmental cell uses a large electron window requiring a support structure underneath the suspended graphene. (b) Mechanical deformation of a sealing graphene membrane as a consequence of pressure difference Δp between the inside and outside of the environmental cell. The high mechanical stability of graphene allows substantial pressure differences Δp , which decrease for larger hole diameters (see text).

spectroscopic photoemission and low-energy electron microscope (SPELEEM), which is described elsewhere [55, 56]. All graphene samples were grown on Cu foils by CVD using a $\text{CH}_4 + \text{H}_2$ atmosphere inside a quartz glass tube that served as a hot wall reactor. The experimental details of the setup can be found elsewhere [57, 58]. Over the reviewed time period, the applied CVD protocols for graphene synthesis were varied, as outlined in section 4 of the manuscript. Three types of protocols were applied, consisting of three different Cu foil pre-treatment steps A, B and C, followed by the actual CVD graphene growth process. The pre-treatment essentially specifies the chosen atmosphere to which the Cu foils are exposed during heating up of the reactor until the desired CVD growth temperature is reached. The chosen parameters of the pre-treatment are listed in table 1. Adding the actual CVD growth to the chosen pre-treatment step leads to the synthesis protocol, which is abbreviated in this manuscript as A + CVD, B + CVD and C + CVD, accordingly. Note that the key ingredient of the improved synthesis protocols B + CVD and C + CVD is to expose the Cu foils to an Ar flow at 1 mbar, to which O_2 with a well-defined partial pressure of 7.5×10^{-6} mbar is added before the CVD process atmosphere is applied.

The techniques used for the transformation of CVD-grown into freestanding graphene are discussed in a separate section of section 5. Here, three different transfer techniques were used. They are abbreviated as T-A, T-B and T-C in this manuscript. A detailed description of the chosen pre-treatment followed by the applied CVD parameters for the growth of all samples shown in this publication are provided as supplementary material (available online at stacks.iop.org/JPD/54/234001/mmedia), also including details regarding the applied transfer protocol.

3. Ultimate goal of environmental PES and mechanical stability limit of sealing graphene membranes

Figure 1(a) sketches the ultimate goal of the environmental cell approach toward photoelectron spectroscopic studies aiming at characterizing vacuum-incompatible samples, such as catalysts surrounded by a high-pressure or liquid environment. An electron transparent window has to be developed that seals an environmental cell which can be introduced into any standard ultrahigh vacuum (UHV) chamber. Thus, an UHV system

hosting standard electron analyzer equipment for surface analysis could be turned into an ambient pressure or, more generally, an environmental spectroscopic system. For this purpose, a large electron transparent window is required to guarantee a sufficiently high signal when using non-focusing irradiation sources. We target the goal of constructing an electron window with a diameter of 2 mm because monochromatic x-ray sources provide light spots of similar size (e.g. Scienta Omicron XM1000 [59], SPECS Focus 500/600 [60], VG-Scienta MX 650 [61]), although non-synchrotron-based systems are on the market that reach a lateral resolution well below 1 mm [62]. When considering the mechanical stability of graphene, it is clear that electron windows of 2 mm diameter require a support structure that stabilizes the sealing graphene membrane.

The requirements regarding mechanical stability are best understood when calculating the mechanical stress on a bulged membrane on top of a pressurized cavity sealing its circular opening of diameter $2a$ as sketched in figure 1(b). The pressure difference Δp stretches the membrane toward the vacuum side of the cavity with the membrane sticking out by a distance δ . The problem of determining the acting stress dependent on the pressure difference has been solved by Briscoe and Panesar by assuming that a membrane of thickness t follows the shape of a spherical cap with radius R as sketched in figure 1(b) [63]. Although it has been noted that there are shortcomings of this model [64], it delivers all essential numbers required for the discussion. The membrane stress σ in the center of the spherical cap amounts to

$$\sigma = \frac{\Delta p R}{2t} \quad (1)$$

with the cap radius R :

$$R = \left[\frac{a^2 E t}{3 \Delta p (1 - \nu)} \right]^{1/3}. \quad (2)$$

Here, E is the elastic modulus and ν expresses the Poisson number of the strained membrane material. We can relate the spherical cap radius R to the vertical deflection δ in a second-order Taylor expansion as $\delta = a^2/2R$ (see supplementary material). The insertion in equation (2) relates the overpressure Δp inside the environmental cell to the vertical displacement of the bulged membrane as

$$\Delta p = \frac{8}{3(1-\nu)} \frac{E t \delta^3}{a^4}. \quad (3)$$

Equation (3) provides the scaling of the pressure difference with the cell window radius and the vertical displacement of the membrane at a given elastic modulus, thickness t and Poisson number ν of the strained membrane. Note that the same scaling relation was extracted by Koenig *et al* in their study based on Hencky's solution of circular membranes [65]. The authors verified the scaling by measuring the vertical deflection of a sealing membrane as a function of the pressure difference of a pressurized cavity with circular opening and even reported an almost identical pre-factor. While equation (3)

delivers a pre-factor of 3.17 for a Poisson number of $\nu = 0.16$, Koenig *et al* derived 3.09 from Hencky's solution [65].

Combining equations (1) and (2) or (1) and (3) relates the overpressure Δp or the vertical deflection δ of the pressurized cavity to the stress σ in the membrane, allowing us to calculate the mechanical stability limit of the membrane assembly:

$$\Delta p = \frac{t}{a} \sqrt{24 \sigma^3 \frac{1-\nu}{E}} \quad (4)$$

or

$$\delta = a \sqrt{\frac{3}{2} (1-\nu) \frac{\sigma}{E}}. \quad (5)$$

Note that equation (4) delivers almost identical values to the formula used by Wang *et al* for their stability analysis of inward deflection of graphene membranes when sealing circular cavities that are exposed to negative pressure [53]. As seen in equation (5), the maximum deflection of the graphene membrane before rupture can be calculated by inserting the Poisson number ν and the σ/E ratio of graphene at maximum possible expansion. Due to the extreme mechanical stability of graphene with $\sigma_{\text{limit}} > 100$ GPa and E of about 1 TPa, the ratio amounts to 0.1 [5, 66]. Using a Poisson number of about $\nu = 0.16$ for strained graphene [66], equation (5) delivers a maximum deflection $\delta_{\text{max}} = 0.35a$ before rupture. In the already mentioned study of Koenig *et al*, exfoliated graphene was used as the sealing membrane on top of a circular cavity hole with $a = 2 \mu\text{m}$ radius. A vertical displacement δ of about 200 nm was measured when pressurizing the cavity by about 4 bar, which matches the predictions of equation (3) reasonably well when inserting $E = 1$ TPa and choosing the graphite layer distance $t = 3.35 \times 10^{-10}$ m [67] as the membrane thickness of monolayer graphene. Koenig *et al* showed in their study that this situation relates to a cavity pressure well below that required for delamination of the graphene sealing and to the case where the vertical displacement of the membrane over the cavity hole can be fitted according to Hencky's solution [65]. Thus, we can consider the vertical displacement of $\delta = 0.1a$ as a safe operation condition of a defect-free graphene membrane that seals a pressurized environmental cell. Assuming a spherical cap geometry of the membrane, we can calculate the uniaxial expansion of the membrane as $\arcsin(2\delta/a) / (2\delta/a)$. Inserting the safe operation conditions of $\delta = 0.1a$ delivers a moderate uniaxial strain of 0.7% whereas the maximum deflection before rupture at $\delta_{\text{max}} = 0.35a$ relates to an enormous nominal strain of 11%.

We can now predict the safe working pressure of graphene-sealed electron windows of a given size. Inserting the safe deflection condition of $\delta = 0.1a$ in equation (3) shows that a cavity with a hole diameter of 1 μm can be pressurized by about 20 bar without membrane rupture. Consequently, a 10 μm -sized hole should withstand 2 bar, a 100 μm hole 200 mbar, and a 1-mm-sized hole could be safely operated at a cell pressure of 20 mbar. Note that the δ^3 scaling in equation (3) allows us to nominally increase the pressure by a factor of 3.5³ when using $\delta_{\text{max}} = 0.35a$ instead of $\delta = 0.1a$, which amounts to a factor of about 43. Due to the reduced elastic

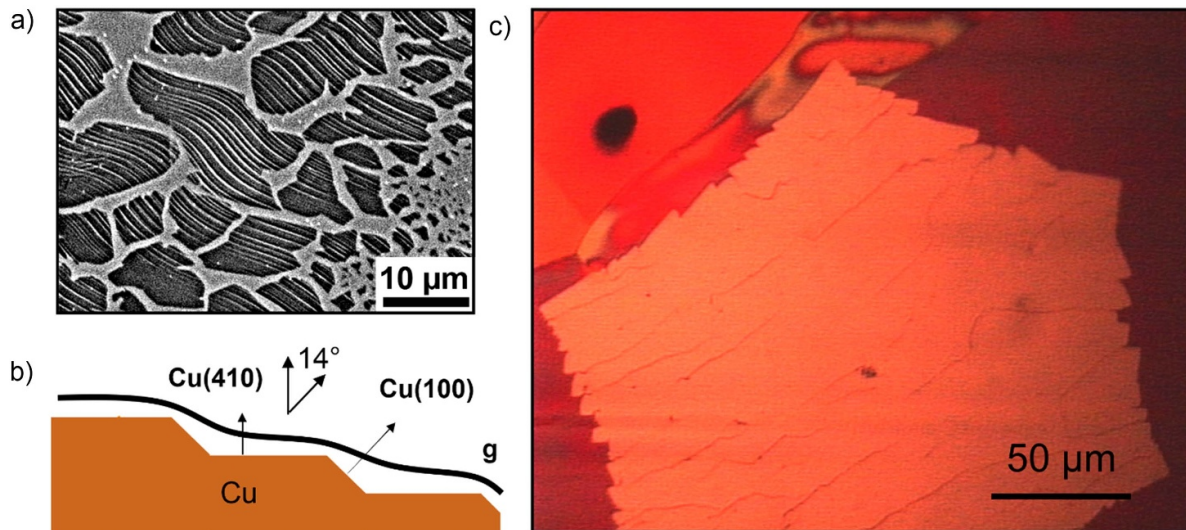


Figure 2. (a) With one year of experience after starting the growth of graphene on Cu by CVD in 2011, we managed to grow polycrystalline monolayer graphene films with single-crystalline grains of a few μm in diameter resulting from the mean size of the growing graphene flakes which appear dark in the SEM image (primary energy 10 keV). It was realized that the Cu foil tends to facet during CVD growth, which accounts for the observed striped appearance of the grown flakes. (b) Using highly (100) textured support Cu foils, we identified a staircase morphology underneath the monolayer graphene film, in particular consisting of an alternating sequence of (410) and (100) planes [57]. (c) An improved pre-treatment of the used Cu foils allowed us to increase the graphene flake size [58]. The optical image shows a single-crystalline monolayer graphene flake of 200 μm diameter. Used growth protocols: (a) A + CVD, (c) B + CVD; for details see supplementary material.

modulus E of graphene at extreme expansion [66], the maximum possible pressure before membrane rupture would be rather half of this value, i.e. a pressure about 20 times larger before membrane burst might be possible. In any case, even when daring to enter the region with highly deformed membranes, the estimated numbers clearly indicate that electron windows of environmental cells with diameters in the mm range will need a support structure when aiming at operating the cells at ambient pressure.

4. Growth of graphene on Cu by CVD

After the self-limiting growth of monolayer graphene by CH_4 decomposition on Cu was reported [68], this CVD protocol turned out to be one of the most promising routes toward this highly wanted material. Following this synthesis strategy, we have produced graphene on Cu foils since 2011 in an attempt to improve the crystalline quality of the material and convert it into freestanding graphene membranes. The polycrystalline nature of CVD-grown graphene films was rapidly identified and it soon became clear that rotational grain boundaries in the resulting membranes are areas where graphene films tend to rupture long before exceeding their nominal mechanical stability limit [69, 70].

4.1. Growth of polycrystalline graphene and staircase morphology of Cu support foils

Following synthesis recipes reported by Li *et al* at that time [68, 71] led to the growth of μm -sized single-crystal graphene flakes on Cu. When applying such growth conditions, it was

found that graphene growth on Cu foils is very often accompanied by a faceting of the Cu support [72, 73], which was also observed by us [57]. Figure 2(a) displays a SEM image of μm -sized graphene islands (so-called flakes) grown on top of a Cu foil following the A + CVD growth protocol (see supplementary material). The graphene flakes are imaged in SEM with a striped appearance. We managed to assign the stripes to alternating inclined surfaces on the Cu support foil. As a special case we could determine the inclination angle of the alternating surface planes to be 14° and identify an alternating sequence of Cu(410) followed by Cu(100) planes on the Cu foil. The sequences of the two Cu planes inclined by 14° were shown to follow a staircase morphology that proceeded on a mesoscopic μm -length scale as sketched in figure 2(b). We also showed that the orientation of the staircase morphology was not correlated to the crystalline alignment of the rotational domains in the grown polycrystalline graphene film [57]. The observed Cu foil restructuring was found to generally occur after graphene synthesis, although typically, foil morphologies with more complicated faceted Cu surfaces appear and the faceting depends on the crystal grain of the polycrystalline Cu foil.

4.2. Improving the crystalline quality of CVD-grown graphene

Besides investigating the foil restructuring of the Cu foil support during CVD growth, much work was invested to improve the crystalline quality of the grown polycrystalline graphene films. Here, two strategies can be followed: either one tries to nucleate at best only one graphene flake on the Cu foil, which then naturally grows as single-crystalline graphene, or one tries to induce the nucleation and growth of many graphene

flakes with aligned graphene lattices and hope that they merge without producing defects in a so-called seamless stitching mode [74, 75]. While both growth strategies are followed in the literature, we focus on the first one, trying to nucleate the least amount of graphene flakes and grow them to the maximum possible size.

It was found that special pre-treatments of the Cu foils before graphene CVD growth greatly reduce the nucleation density of graphene islands during CVD synthesis and thus enable the growth of large, single-crystalline graphene flakes [76–78]. In particular, treatments in oxygen-containing atmospheres turned out to guarantee low graphene flake nucleation. Successful protocols include applying an oxidative Cu foil pre-treatment [79] or oxygen exposure during the annealing step of the Cu foil and/or during CVD growth [78, 80, 81]. The latter is often achieved by adding argon to the reactive gas mixture, making use of the oxygen impurity, which amounts to a few ppm in 5.0 argon. In addition, the consumption of oxygen from the Cu foil bulk was used [79] or, as observed later, an oxygen flow from an oxygen-releasing solid placed below the Cu foil [82] can be used to guarantee a low nucleation rate of graphene flakes during CVD growth.

We were able to establish an oxidative pre-treatment experiment where the amount of impinging oxygen molecules was precisely controlled so that the impingement events could be counted atom by atom. Being able to determine the carbon content of the Cu foil by a segregation-type experiment, we could show that during the oxidative Cu foil pre-treatment the amount of volume dissolved and segregating carbon in the Cu foil is reduced, which goes hand in hand with the reduced graphene nucleation during CVD growth [58]. Once it was known that the carbon content in the foil greatly exceeds the amount expected in thermodynamic equilibrium, we interpreted that, during the Cu foil-milling manufacturing process, carbon-containing material is mechanically pressed into the foil, an interpretation which was later verified by Braueninger *et al* in a secondary ion mass spectroscopy study [83] and which was also noted recently by Luo *et al* [84].

Figure 2(c) shows the outcome of the upgraded CVD process, making use of an oxidative pre-treatment of the Cu foil before adjusting the actual CVD graphene growth (B + CVD growth protocol; see supplementary material) [58]. Figure 2(c) displays an optical image of a grown graphene flake with a 200 μm diameter. The contrast in the optical image was achieved by heating the g/Cu sample on a hot plate in air in order to locally oxidize the bare Cu foil as reported in the literature [76]. Since graphene protects the Cu foil from oxidation, only the uncovered areas change to the red color of copper(I) oxide while the Cu foil underneath the graphene flakes remains unchanged.

The CVD growth of graphene on Cu may be even further optimized by turning the Cu foil into a quasi-single-crystalline substrate by prolonged annealing in Ar/H₂ [75]. Reckinger *et al* also reported an appropriate pre-treatment consisting of an annealing ramp in an oxygen-containing gas atmosphere followed by a sudden reduction step, which not only suppresses the graphene flake nucleation during the

subsequent CVD growth process but also leads to the conversion of Cu foil into an almost entirely (111)-textured substrate foil [85]. The recipe is meanwhile improved and a special contact-free annealing of Cu foils provides quasi-single crystalline Cu(111), which can then be used as a support for CVD growth of graphene [86]. We also apply a variant of this Cu foil pre-treatment, which increases the amount and size of (111)-oriented grains in the Cu foil and enables us to grow mm-sized single-crystalline graphene flakes on an almost entirely (111)-textured Cu foil (C + CVD protocol; see supplementary material).

4.3. Quasi-single-crystalline graphene on extended Cu(111) grains: quantum oscillations, graphene lattice alignment and staircase support morphology

Figure 3 shows LEEM data obtained after applying the B + CVD growth protocol in our reactor setup. After insertion of the Cu foil in the reactor, the sample was annealed in hydrogen followed by exposure to a highly diluted oxygen flow in Ar of about $1 \div 10^{-5}$. After the mild oxidative pre-treatment of the Cu foil, the actual CVD graphene growth was performed at 1050 °C, which led to the formation of monolayer graphene almost entirely covering the Cu foil, which was not completely (111)-textured (as expected following the C-CVD protocol) but already contained extended grains, with the majority being (111)-oriented. Bright-field LEEM images recorded from this surface are shown in figures 3(a) and (b). The image contrast results from the electron reflectivity of the (0,0) beam at the given start voltage energy, which amounted to 2.5 eV and 7.5 eV for the images shown in figures 3(a) and (b), respectively. Note that the start voltage energy is equal to the kinetic electron energy offset by the mirror electron microscopy (MEM) transition energy, which amounted to 0.6 eV in the displayed data set. Both images show a bilayer graphene island with a diameter of about 20 μm inside the continuous monolayer graphene film on top of the Cu foil. Bilayer graphene islands cover a surface fraction of less than 10% when applying the above-mentioned CVD growth conditions and, thus, represent a minority species in the graphene film. The bilayer graphene island appears with reversed contrast in the two different LEEM images of figures 3(a) and (b). We can record a whole data set of LEEM images as a function of increasing kinetic electron energy and extract the reflected intensity of the imaged areas covered by mono- and bilayer graphene. The result of this so-called LEEM *I/V* analysis is plotted in figure 3(c). The arrows in the plot indicate the energies at which the images in figures 3(a) and (b) were acquired, explaining the observed contrast reversal in the image. As clearly seen in the chart, the (0,0) electron beam reflected from monolayer graphene on Cu shows an *I/V* curve which is almost featureless, while the one taken from the bilayer graphene island has a pronounced dip at 2.5 eV followed by an intensive reflectivity increase at about 10 eV. The intensity oscillations at low electron energies have been attributed to quantum oscillations of the electron wave function inside the layered graphene material with n minima relating to $(n + 1)$ graphene layers. Thus, we can safely attribute the observed hexagonal island to bilayer

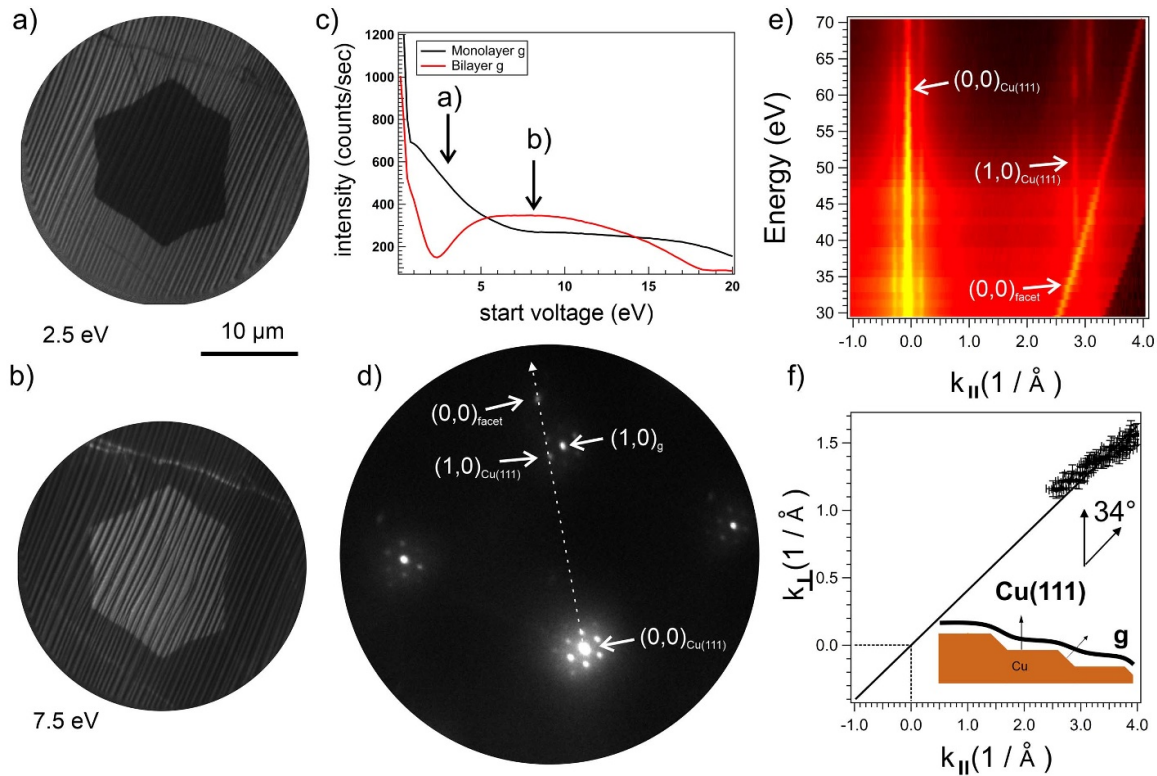


Figure 3. Cu foil pre-treatment and CVD growth following the B + CVD protocol led to the formation of monolayer graphene with large single-crystalline domains on a highly (111) textured Cu. (a) A bilayer graphene island surrounded by the continuous monolayer film imaged by LEEM at 2.5 eV. (b) The same area imaged at 7.5 eV. (c) Variation of the reflected (0,0) beam intensity as a function of the start voltage energy derived by evaluating the pixel intensity of the monolayer and bilayer phase from LEEM images that were acquired at the respective start voltage energy (LEEM *I/V* image analysis). Arrows indicate the energy at which images (a) and (b) were acquired and explain the observed contrast. (d) Diffraction pattern acquired from monolayer g/Cu at 60 eV. Moiré diffraction spots in addition to the identified $(0,0)_{\text{Cu}(111)}$, $(1,0)_{\text{Cu}(111)}$ and $(1,0)_g$ peaks indicate a slightly rotated graphene lattice on a Cu(111) surface (see text). In addition, diffraction spots appear that relate to electron reflection from an inclined Cu facet. The indicated $(0,0)_{\text{facet}}$ spot relates to a reciprocal scattering vector that contains a k_{\parallel} component causing the spot movement along the dotted line with increasing electron energy. (e) Intensity cuts along this direction displayed as waterfall plot with the electron energy as vertical axis, the k_{\parallel} vector component as horizontal axis and the spot intensity using false color coding (see text). (f) Converting the beam energy into the respective k_{\perp} value leads to the linear plot through the coordinate origin (see dotted lines) from which an inclination angle of 34° of the facet with respect to the Cu(111) plane can be extracted. The two surface planes account for the striped appearance of the LEEM images of (a) and (b). The k -values shown in (e) and (f) follow the reciprocal space notation including the factor of 2π .

graphene and the surrounding area to monolayer graphene on top of the Cu foil substrate [87]. Apart from the contrast of the bilayer graphene island, the LEEM images of figures 3(a) and (b) show a sequence of regular stripes proceeding from the lower left to the top of each image. Further below, we will discuss how these stripes relate to differently aligned Cu surface planes, similar to the case already shown in figure 2. The irregular line above the bilayer graphene island is a so-called wrinkle where the graphene film is folded. Accordingly, the folding of the monolayer graphene along the wrinkle leads to the same contrast as the bilayer graphene island.

The low-energy electron diffraction (LEED) pattern was recorded from an area selected spot of the Cu foil covered by monolayer graphene using the so-called μ -LEED operation mode of the SPELEEM instrument [56]. An image recorded at a kinetic electron energy of 60 eV is shown in figure 3(d). The diffraction pattern displays pronounced moiré spots surrounding the (0,0) and first-order beams. The hexagonal moiré pattern clearly identifies the local Cu support

as a single-crystal grain with its Cu(111) surface plane aligned perpendicularly to the optical axis of the microscope. The Cu(111) surface is covered by a slightly rotated graphene lattice as indicated by the identified $(1,0)_g$ and $(1,0)_{\text{Cu}(111)}$ diffraction spots of the diffraction pattern shown in figure 3(d) [88].

4.4. Extracting the angle between inclined surface planes of the staircase

The LEED pattern not only shows the diffraction spots of the g/Cu(111) surface plane but also displays additional diffraction spots and especially the identified (0,0) beam, which originates from the specular electron reflection from an inclined surface facet. This spot is indicated as the $(0,0)_{\text{facet}}$ in the graph, accordingly. Diffraction spots caused by the reflection from an inclined surface plane are easily identified in a LEEM apparatus when recording the diffraction pattern at varying kinetic electron energy. According to the imaging properties

of a LEEM instrument, diffraction spots of an aligned surface plane remain at a fixed k_{\parallel} -space position of the recorded diffraction pattern when varying the kinetic electron energy, while spots originating from an inclined surface move along a certain direction within the k_{\parallel} plane. Recording the movement as a function of the electron kinetic energy can be used to determine the inclination angle [89]. The dotted line in figure 3(d) indicates the direction along which the $(0,0)_{\text{facet}}$ spot moves with increasing energy. Careful inspection shows that the dotted line intersects the $(1,0)_{\text{Cu}(111)}$ diffraction spot. This finding identifies that the inclination of the facet originates from a plane which is rotated with the densely packed $\langle 1\bar{1}0 \rangle$ direction of the Cu(111) lattice as the rotational axis. As a result, the facet must be an $\{m\ n\ n\}$ or an $\{m\ m\ n\}$ surface plane depending on whether the inclination of the facet proceeds toward the $\{011\}$ or toward the $\{001\}$ crystal plane.

The inclination angle can be determined when following the k_{\parallel} -space position of the $(0,0)_{\text{facet}}$ spot along the dotted line as a function of kinetic energy, similar to the analysis performed in our study relating to the data shown in figure 2 [57]. The analysis of the inclination angle φ with respect to the optical axis of the microscope can be performed for the $(0,0)$ diffraction spot by using the k -space relation for the $(0,0)$ spot under specular reflection as

$$\tan(2\varphi) = \frac{k_{\parallel}}{k_{\perp}}. \quad (6)$$

In order to derive the inclination angle φ , the spot profiles are extracted as the intensity versus k_{\parallel} -position curve along the dotted line of the diffraction pattern acquired at the electron energy E and each curve is plotted in a 2D chart with E as the vertical and k_{\parallel} as the horizontal axis while color coding the spot profile intensity with high (low) intensity appearing bright yellow (dark red). The resulting so-called waterfall plot is shown in figure 3(e) and displays the $(0,0)_{\text{Cu}(111)}$ and the $(1,0)_{\text{Cu}(111)}$ peak position at a fixed k_{\parallel} position while the $(0,0)_{\text{facet}}$ diffraction spot moves as a function of kinetic energy along the k_{\parallel} direction. Converting the kinetic energy to the corresponding value of k_{\perp} allows us to plot the $(0,0)_{\text{facet}}$ spot position in the k_{\perp} vs k_{\parallel} chart displayed in figure 3(f). In this plot, the $(0,0)$ spot has to move along a straight line through the coordinate origin with a slope of $1/\tan(2\varphi)$ with φ as the angle of the inclined surface plane. The analysis verifies the existence of a plane highly inclined by 34° . This number almost matches the inclination angle of 35.3° , which would indicate either a (110) or a (411) surface plane.

The performed analysis proves that, although the improved CVD growth protocol induced the formation of an extended Cu(111) grain that is entirely covered by single-crystalline monolayer graphene, the restructuring of the Cu support surface is still observed. Comparison of figures 2 and 3 shows that in both cases a staircase-type morphology of the Cu foil exists, consisting of a regular sequence of two Cu planes that are inclined with respect to each other. The covering monolayer graphene film follows the staircase morphology, regardless of whether the graphene is poly- (figure 2) or single-crystalline (figure 3). The morphology of CVD-grown graphene on Cu

proceeds on the μm -length scale as seen from the real-space LEEM data, which has an enormous effect on the properties of freestanding graphene obtained after detaching the grown film from the Cu support.

5. Transfer protocols

Two different approaches were used to separate the CVD-grown graphene layer from its support surface. While the mechanical separation following the so-called ‘bubbling transfer method’ [90, 91] conserves both the substrate and the 2D layer (as seen in path [a] in figure 4), the etching separation approach is based on dissolution of the substrate layer, leaving the single 2D layer behind (shown in path [b] in figure 4).

When mechanically separating the graphene from the substrate, significant stress acts on the graphene film, which is typically stabilized by a protection layer. This is commonly a polymer layer, such as poly-methyl-methacrylate (PMMA) or polycarbonate (PC), which is spin-coated on the sample to achieve a continuous layer of a few 100 nm thickness [92] (step II in figure 4). The bubbling transfer method uses the electrolytic water splitting in an electrolyte solution to create hydrogen gas at the copper surface, which smoothly lifts off the graphene/protection layer stack from the substrate (step III [a] in figure 4). This technique preserves the substrate material, which allows precious substrate materials such as Pt to be used, on which graphene can also be grown [91]. The electrolyte solution itself, commonly a sodium hydroxide solution (NaOH (aq.)), can simply be exchanged by water to remove NaOH residues (step VI in figure 4), followed by the fishing of the graphene/protection layer stack with the desired substrate. For our purpose, a holey grid or a single-hole aperture is used as the target support (step V in figure 4). The protection layer can be removed after the transfer process by dissolution in cold or hot acetone (step VI in figure 4) followed by a sample drying procedure (step VII in figure 4). The last two preparation steps toward freestanding graphene impose additional stress on the membrane when removing the protective layer and also affect the cleanliness of the resulting membrane surface. Therefore, alternative recipes are reported in the literature that try to avoid or at least reduce these shortcomings. For example, instead of PMMA, anthracene was used as the protective layer, which can be easily sublimated from the membrane after the transfer process without immersion into a solvent, avoiding the variation of the surface tension when drying the exposed membranes after removal from the solvent [93]. Other approaches slowly exchange the used solvent by liquids with extremely low surface tension or dry the sample by passing over the critical point of the solvent, avoiding a sudden phase change [49, 94]. In addition, a preparation step including the pressure or heat-induced softening of the protection layer was introduced in the transfer protocol between steps (V) and (VI) in order to facilitate graphene adhesion with a maximized support contact area, avoiding the delamination of the transferred membrane during protective layer removal [95–97].

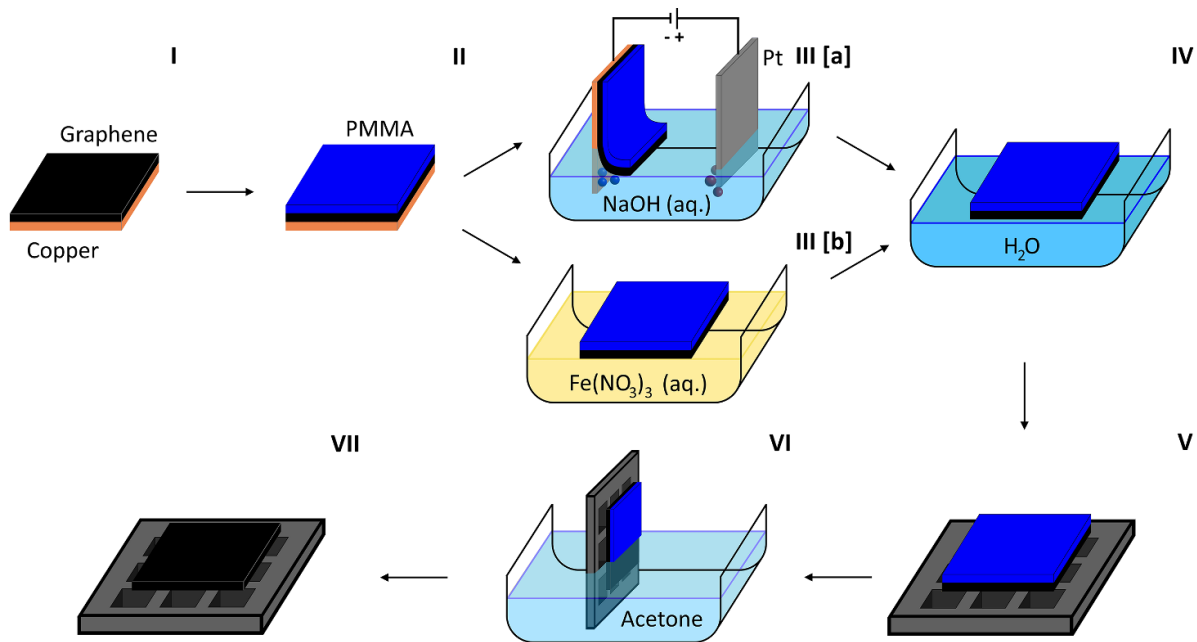


Figure 4. Simplified protocols to detach the CVD-grown graphene from the Cu substrate and transfer it onto a new target support: after CVD growth on Cu (I) a PMMA protection layer is spin-coated on top of the grown graphene film for mechanical protection (II). The release from the Cu foil is either done by electrochemical separation, using the so-called bubbling transfer process (III[a]) or by chemically dissolving the Cu foil (III[b]). The decoupled graphene/polymer stack floats on the solution, which is subsequently exchanged with purified water (IV). A new target support is used to fish the stack (V). Finally, the protection layer is washed off in acetone (VI) and the remaining graphene on the support structure is dried in air (VII). Several modifications of the transfer scheme have been reported in the literature and were also applied by us (see text).

When using the etching separation approach, the forces acting on the graphene layer during the dissolution of the metal substrate are much weaker than in the equivalent bubbling transfer step (step III [b] in figure 4). This allows for the use of thinner polymer layers or even deposited nm-thick metal films instead of spin-coated polymers as the protective layer [94], which allows for a better adhesion of the transferred stack on the target substrate. It is even possible to remove the Cu substrate below the unprotected CVD-grown graphene. This is achieved by applying a stabilizing frame around the target graphene area [44, 98] or by contacting the destination target on top of the CVD-grown g/Cu sample before the start of the etching procedure [99]. We also managed to electrically contact the g/Cu foil with a thin cable while floating on a NaOH(aq.) electrolyte solution and then locally electrochemically etch holes underneath the unprotected graphene in the lithographically pre-structured backside of the Cu support (see [57] and also figure 5(a)). As an alternative to electrochemical etching, chemical dissolution of the Cu support foils is also possible and has been reported using an aqueous iron(III) nitrate ($\text{Fe}(\text{NO}_3)_3$ (aq.)) [100], iron(III) chloride (FeCl_3 (aq.)) [101] or ammonium persulfate ($(\text{NH}_4)_2\text{S}_2\text{O}_8$ (aq.)) [97]. Due to the greater flexibility in choosing the protection material (or none at all), the success rate of etching-based transfer methods is commonly higher than that of bubbling transfer approaches, and it is possible to span larger holes. A significant drawback is nevertheless that by dissolving the complete substrate structure, impurities originating from incomplete etching of the metal substrate foil and

from the etching solution itself may be found on the graphene membrane [48].

After successful production of freestanding graphene membranes, these are still contaminated by residues of the protection layer and impurities from the encapsulated solvent and—if applied—from the etching of the substrate. These contaminants can be reduced by heating the sample in air in the presence of activated carbon to adsorb any released organic residues [102] or heating the sample after the deposition of platinum nanoparticles acting as a catalyst for the reaction of impurities with oxygen from the air [93]. Creating samples compatible with ultrahigh vacuum conditions additionally requires an annealing step in the vacuum to desorb any contaminants from the sample with a significant vapor pressure [49].

We applied essentially three different transfer protocols when producing the freestanding graphene membranes shown in this publication: bubbling transfer of PMMA-protected graphene, dissolution of Cu in $\text{Fe}(\text{NO}_3)_3$ (aq.) underneath the PMMA-protected graphene, and the same Cu dissolution transfer protocol but without a PMMA protective film or with the help of a stabilizing PMMA frame surrounding the unprotected graphene area to be transferred. The latter transfer is similar to the protocol described by Weatherup [98]. Following this recipe, a PMMA frame was applied around the graphene-covered area instead of covering the entire graphene with a continuous polymer film. The supporting PMMA frame is stabilizing enough to prevent rupture of the film and allows for perfect adaptation to the fishing target. After transfer, the outer, stabilizing PMMA frame can be removed manually with

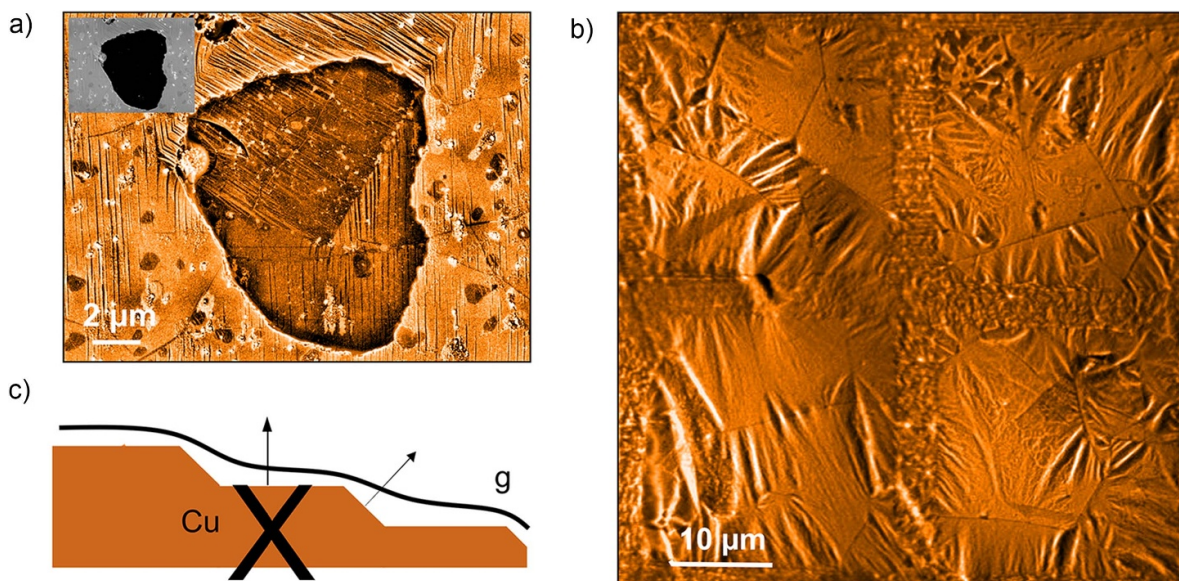


Figure 5. Membrane morphology for freestanding graphene. (a) SEM image of a Cu foil covered by monolayer graphene with a hole locally etched into the Cu support (primary energy 5 keV). The inset clearly shows the hole. Contrast enhancement of the respective areas in the SEM image verifies that the hole is covered by graphene, which still reflects the morphology of the former Cu foil. (b) LEEM image (acquired at 0.7 eV) confirms that the Cu foil morphology is imprinted in the graphene film even if the graphene is completely removed from the Cu support and placed onto a grid with 20 μm-sized holes. (c) The sketch indicates the staircase morphology of the support covered by the CVD-grown graphene layer. The imprinted morphology of the graphene film remains even when removing the solid Cu support. (Growth protocol: (a) A + CVD, (b) B + CVD. Transfer protocol: (a) local etching without PMMA, (b) T-A, see supplementary material).

tweezers and does not require PMMA dissolution in acetone. Nevertheless, rinsing in acetone was typically subsequently added in order to remove the remaining soluble organic impurities. In the following, the transfer protocols are abbreviated as T-A = transfer using an entire PMMA layer, T-B = transfer with a PMMA frame, and T-C = bubbling transfer; further details regarding the applied transfer protocols are provided as supplementary material.

6. Membrane morphology and crystal structure of freestanding graphene

Having shown in the previous sections that single-crystalline graphene can be grown by CVD, which can then be detached from the Cu support, we turn our focus to the properties of the resulting membrane material. In section 4.3 it was already shown that CVD-grown graphene is well defined on the atomic scale with the known hexagonal honeycomb lattice of monolayer graphene. Apart from this, CVD-grown graphene follows the staircase morphology of the Cu foil support, which restructures on the micro-meter length scale during CVD synthesis.

6.1. Preserved staircase morphology of freestanding-CVD grown graphene

We will now discuss what happens if the supported graphene is converted into a freestanding graphene membrane. This effect is best observed in figure 5(a), which displays a SEM image with the contrast reflecting the secondary electron emission from monolayer graphene on a Cu foil. The film was

grown according to the A + CVD preparation protocol until a continuous graphene film was formed on the Cu foil, which was polycrystalline and mainly monolayer thick. After CVD growth, the sample was placed in a special electrochemical etching setup that allowed the Cu support underneath the grown graphene to be locally removed [57]. The inset displays the SEM image of an area where a hole with a diameter of about 10 μm was locally etched underneath the graphene film. By using a linear gray scale, the hole appears black while the surrounding graphene-covered Cu appears bright. When instead applying a special contrast enhancement that provides contrast on the surrounding Cu and on the hole at the same time, the SEM image appears as the displayed large image of figure 5(a). The contrast enhancement on the graphene-covered Cu foil surrounding the etched hole shows several features that have to be discussed. A few small dark islands are randomly distributed on the Cu surface, which we identified as being bi- or multilayer bilayer graphene islands that cover an area of <5% of the monolayer graphene film. The imaged area of the Cu foil is completely covered by the grown monolayer graphene film which is confirmed by SEM at boundaries to the uncovered Cu, which are rarely observed on the sample. Thin lines propagating within the imaged area can be identified as graphene wrinkles that were already discussed in figure 3(a). Finally, the appearance of stripes is clearly observed on the Cu foil. These regularly aligned stripes can be identified as sequences of differently faceted surfaces. The Cu crystal grains affect the alignment of the stripes, which allows us to identify two different Cu grains in the imaged area on which differently aligned facet sequences appear: one Cu grain where the boundary between subsequently inclined

surface planes propagates vertically, whereas the respective stripes propagate as diagonals within the other grain of the Cu foil. Having already identified the imaged stripes as the staircase morphology of the graphene-covered Cu foil that develops during CVD growth, we can now turn our attention to the contrast visible inside the etched hole, which shows two remarkable facts: the presence of any contrast at all indicates that the covering graphene film survived the local substrate etching. Surprisingly, the contrast variation visible on the surrounding Cu foil continues inside the hole area without disruption. This means that the morphology of the former Cu foil support is still imprinted in the freestanding graphene membrane covering the etched hole. This surprising effect is even found when completely detaching the graphene film from the Cu foil and transferring it onto a new support by applying the transfer strategies outlined in section 5.

Figure 5(b) shows a LEEM image of a transferred graphene membrane that has been placed on a support grid with rectangular holes of $20\ \mu\text{m}$ side length. The membrane material was grown by CVD applying the improved protocol B + CVD so that it was capable of covering larger frames. The membrane is imaged with the transferred membrane on top of the grid support. The rectangular frame of the grid is slightly visible where the membrane adheres on the bars of the grid and shows a field of 2×2 holes. The LEEM image was acquired at a start voltage energy of 0.7 eV, which amounted to the so-called MEM transition. In this imaging mode, the contrast emerges from the electron reflection due to the electric field in front of the sample, and thus reflects a mixture of topography and work function variations. As a result, bi- or multilayer graphene islands in the graphene membrane do not lead to image contrast, whereas the membrane morphology is clearly resolved.

Similar to figure 5(a), one can clearly observe the imprinted morphology of the former Cu support foil. Since the graphene layer was grown by CVD according to the growth recipe that does not entirely remove the polycrystalline nature of the Cu foil, one even sees the marks of the former Cu grain in the top-left rectangle, which proceeds diagonally from the top left to the bottom right of the image. In addition, wrinkles are imaged as a thin straight line in the membrane but most importantly, the areas where the former Cu foil developed a staircase morphology during CVD are clearly visible, because the freestanding graphene membrane still mimics this morphology. Figure 5(c) sketches the observation that the staircase morphology of the Cu support is still conserved in the CVD-grown graphene even if the support is dissolved or the membrane is mechanically detached from the support foil. At first sight, this situation seems to be surprising, as one would expect membrane relaxation perpendicular to the steps of the staircase when removing the support. However, while such a motion is possible in a 1D structure, a local staircase embedded in a 2D membrane cannot relax without inducing stress within the surrounding membrane. An extreme example is the membrane morphology that contains two staircases with rotated staircase directions in contact with each other. In such a geometry, relaxation along one staircase direction would

naturally induce straining with respect to the other staircase; thus, it is impossible to relax both staircases into a flat membrane at the same time without applying stress.

6.2. Straining freestanding graphene by thermal expansion of the supporting frame

As a result, we have to conclude that CVD-grown graphene is not flat, even in its freestanding form. This finding might explain why the mechanical resonance frequencies of doubly clamped freestanding CVD-grown graphene show a large variation with respect to the frequency and quality factor of the fundamental vibration mode [103]. It also affects the mechanical membrane properties under static tension, which can be applied when annealing the support frame and induce its thermal expansion, making use of the fact that graphene essentially does not thermally expand [104]. Figure 6 displays two experiments where graphene membranes are annealed together with their supporting frame. In both experiments, a TEM grid made from Cu with $20\ \mu\text{m}$ -wide quadratic holes served as the support structure. The large linear thermal expansion coefficient of Cu of $17 \times 10^{-6}\ \text{K}^{-1}$ [105] induces a substantial strain of the suspended graphene membranes during annealing. Figure 6 displays two annealing experiments of graphene membranes that were fixed on a Cu grid. Both membranes were synthesized by applying the B-CVD growth protocol followed by transfer onto the grid along the T-A protocol (see supplementary material).

Figure 6(a) displays a LEEM image sequence from the annealing of the first sample, recorded at 60 eV from the backside of the membrane with the support grid facing the objective of the microscope (movie provided as supplementary material). In the upper left part of the image, the membrane is highly folded due to the imprinted morphology of the former Cu foil growth substrate. As a result, the membrane covers the frame in a rather floppy geometry. When annealing the Cu grid from room temperature to $320\ ^\circ\text{C}$, the copper support grid expands by 0.5% in each direction of the frame. As seen in the displayed sequence, the folded area in the top left part of the membrane turns flat when reaching $320\ ^\circ\text{C}$. Note that the expansion of the support grid is mostly compensated by this membrane flattening and is, thus, not entirely transferred into in-plane straining of the membrane.

The second example displayed in figure 6(b) shows a graphene membrane that was placed on the support grid in an almost planar geometry. Now, the thermal expansion of the support frame directly transfers into an in-plane straining of the membrane. In this data set, the top side of the transferred membrane is imaged with the grid below the membrane. The field of view shows one division bar crossing of the grid with two bars separating four quadratic holes. The dark hexagonal island is identified as a trilayer graphene island on a local bilayer graphene membrane. The origin of this contrast will be discussed further below. The sequence displays the membrane during annealing from room temperature to $190\ ^\circ\text{C}$ (a movie of the membrane annealing and its subsequent

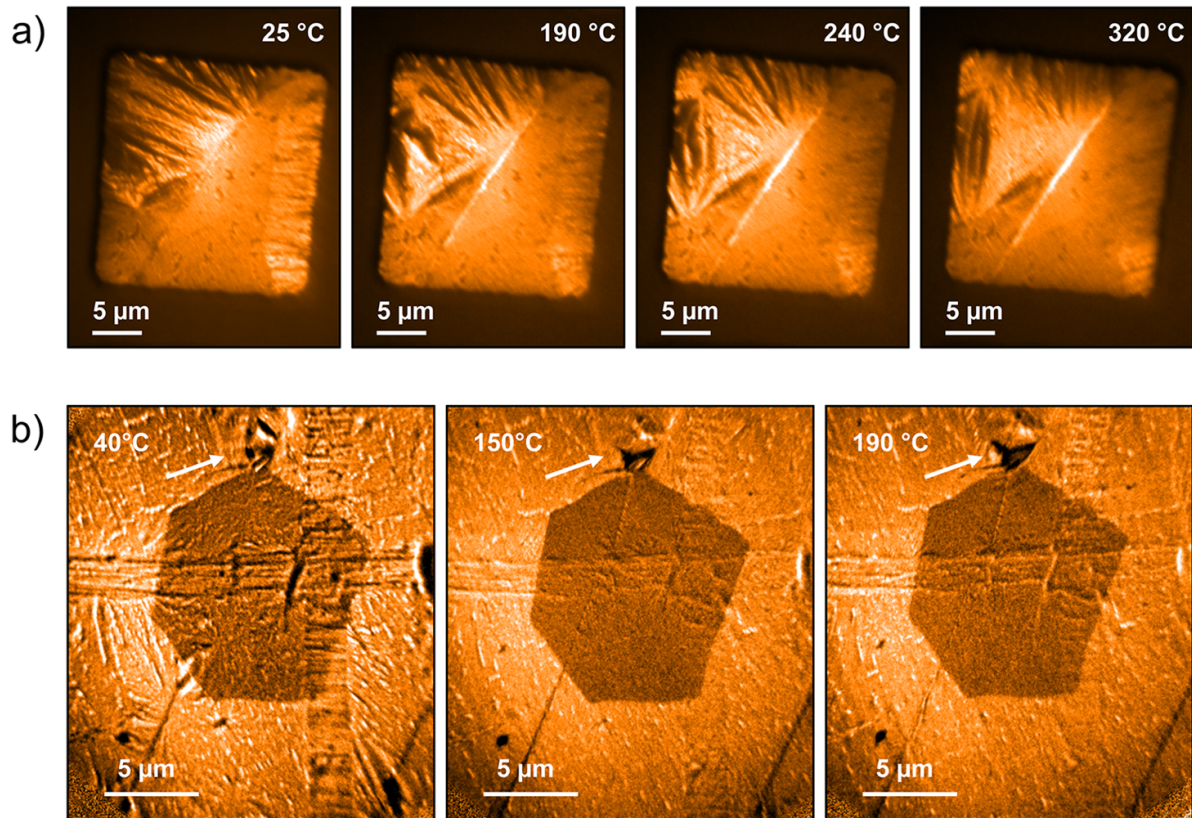


Figure 6. Thermal expansion of the support grid during annealing leads to a straining of suspended graphene that does not thermally expand. (a) Suspended graphene covering the supporting grid in a floppy geometry gradually flattens during annealing. The membrane was imaged by LEEM at 60 eV from the backside of the membrane with the support grid facing the objective of the microscope. (b) Graphene suspended on a support grid in a flat geometry is strained during anneal. The LEEM image sequence is acquired at 0.8 eV from the frontside of the membrane with the supporting grid behind. In the upper part of each image a white arrow indicates a position where the induced stress leads to the rupture of the membrane. The dark hexagonal patch is a trilayer graphene island within a bilayer membrane (see text). Growth and transfer protocol of both membranes: B + CVD and T-A; see supplementary material, where movies of both sequences are also found.

cooling is provided as supplementary material). Due to the flat alignment of the membrane, the thermal expansion of the TEM grid of about 0.3% along the horizontal and vertical direction is transferred into an isotropic straining of the membrane. The graphene membrane should easily withstand this expansion (nominally graphene should resist straining well above 10% [66]). However, if a defect is present in the membrane, the induced strain readily induces rupture of the freestanding graphene. A white arrow points to such a case where the thermally induced strain causes the membrane rupture, leading to a 3 μm-sized hole. Note that defective freestanding graphene ruptures rather than delaminates from the support, which agrees with the reported ultrastrong adhesion of graphene membranes [65]. Keeping the findings of both experiments in mind, it is not clear *a priori* whether a flat or a folded geometry of the membrane is advantageous. For example, if liquids are enclosed in an environmental cell, the vertical movement of the electron window while pumping down the surrounding chamber may help to buffer the pressure decay inside the cell. In fact, the already mentioned pressure relief membranes often placed opposite to the electron window are inserted to intentionally reduce the force acting on the electron window.

6.3. Quantum oscillations in freestanding graphene and the thickness of graphene membranes

The findings of both experiments shown in figure 6 are important because of another fact. When analyzing the crystal structure of freestanding graphene, the samples require thorough annealing and degassing in a vacuum before LEED effects become visible. Thus, the graphene membranes have to withstand the induced stress during annealing, which sorts out the mechanically unstable membranes, before any characterization by LEED can take place.

The already mentioned quantum oscillations of the (0,0) beam reflectivity appear not only in supported graphene as shown in figure 3, but also in its freestanding form as has been observed in suspended, exfoliated graphene [106]. Figure 7 shows that well-defined quantum oscillations are also observed by LEEM in transferred CVD-grown graphene membranes that have been well degassed. The oscillations can be used to determine the number of stacked carbon layers inside the membrane, i.e. they provide a sensitive measure of the membrane thickness. The LEEM image displays freestanding graphene grown by applying the C + CVD synthesis protocol after transfer onto a grid with hexagonally

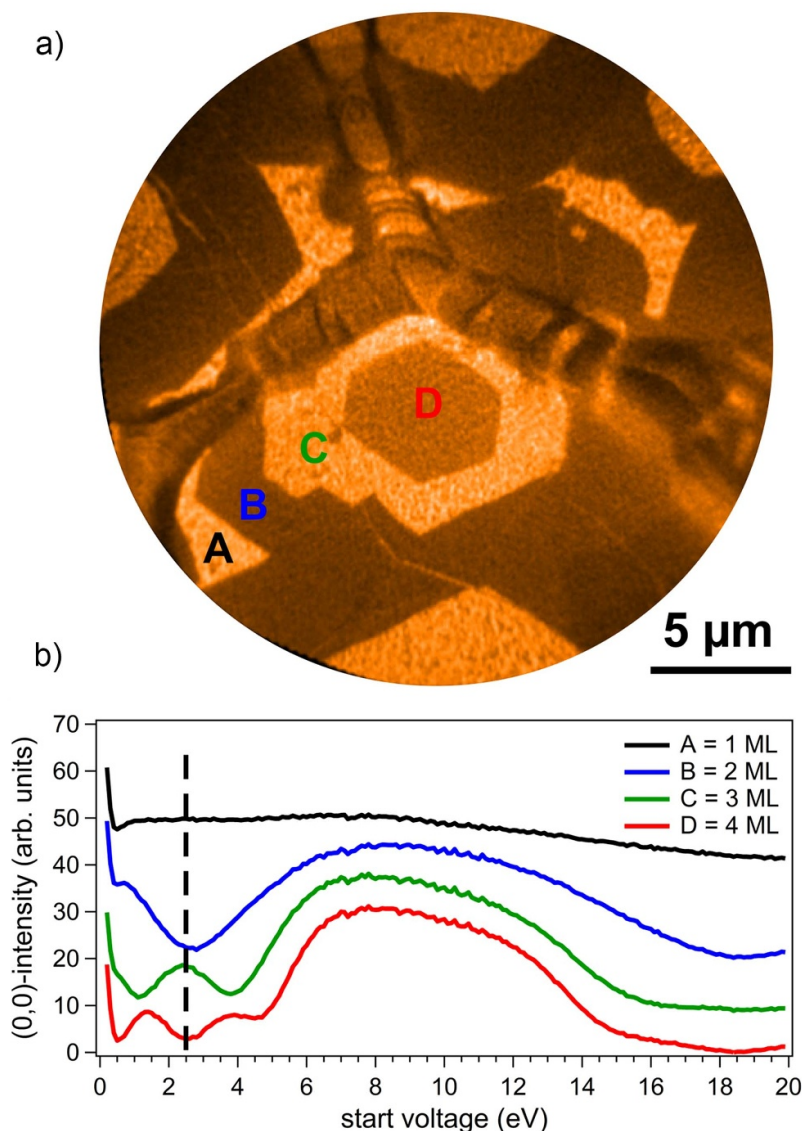


Figure 7. Freestanding graphene film transferred onto a grid with hexagonal holes of $20\ \mu\text{m}$ diameter. (a) The LEEM image taken at $2.5\ \text{eV}$ resolves three bars of the grid and hexagonally shaped patches in the membrane with alternating contrast. Four patches, A, B, C and D, are indicated in the graph. (b) Acquiring a set of LEEM images as a function of start voltage energy, extracting the gray scale intensity from the indicated patches A, B, C and D and plotting them versus the energy leads to the graph below the image. For the purpose of better viewing, the individual plots are displaced vertically with respect to each other. The plots relate to the (0,0) beam reflectivity and show well-defined oscillations within the energy range of (0–6) eV, with n dips in the reflectivity curve relating to $n + 1$ stacked carbon layers in the membrane. Thus, the analysis allows us to verify that the local areas A, B, C and D are made of mono-, bi-, tri- and four-layer-thick graphene. The dashed line in the reflectivity plot indicates the start voltage energy of $2.5\ \text{eV}$, at which image (a) was acquired. Due to the alternation of minima and maxima in the (0,0) beam reflectivity, this energy value is ideal for the acquisition of LEEM images that provide contrast reversal whenever the membrane thickness changes by one carbon layer (growth and transfer protocol for membrane formation: C + CVD and T-B, see supplementary material).

shaped holes of $20\ \mu\text{m}$ diameter following the T-B protocol (see supplementary material). The displayed area shows three crossing bars separating the graphene-covered adjacent holes of the grid. The LEEM image was acquired at a kinetic energy of $2.5\ \text{eV}$ and provides contrast of hexagonally shaped patches on the membrane. Areas with alternating contrast are marked as A, B, C and D in the image from which the image intensity was extracted, which relates to the reflected (0,0) beam intensity. By recording a set of LEEM images as a function of the start voltage energy in a LEEM I/V data set, the electron

reflectivity curve of the indicated areas A, B, C and D was derived and plotted versus the start voltage energy, which is shown in figure 7(b) (note that the start voltage energy is equal to the kinetic electron energy offset by the MEM transition energy, which amounts to $0.6\ \text{eV}$ in the present data set). Well-defined reflectivity oscillations are observed between 0 and 6 eV. Using the fact that n dips in the reflectivity curve can be related to $n + 1$ atomic graphene layers [87], we can determine the local membrane thickness as indicated in the graph. Note that monolayer graphene is clearly identified in area A

not only because of the absence of quantum oscillations within the energy range of 0–6 eV, but because the (0,0) spot intensity does not reflect any constructive interference effect at all, which leads to pronounced Bragg peaks in bi-, tri- and four-layer graphene.

As indicated in figure 7(b), the assignment clearly identifies area A of the membrane as monolayer graphene and B, C and D as bi-, tri- and four-layer graphene. The dashed line in the chart of figure 7(b) at 2.5 eV clearly shows why the contrast reversal in figure 7(a) indicates the stepwise increase in the membrane layer thickness by one graphene layer at a time. The reflectivity curves of figure 7(b) also explain why the trilayer graphene island resolved in the LEEM image sequence of figure 6(b) taken at 0.8 eV appeared darker than the surrounding bilayer graphene membrane.

Note that films that are not well degassed do not show any quantum oscillations in the electron reflectivity at all. Thus, the absence of oscillations in the electron reflectivity curve acquired from freestanding graphene cannot be used to unambiguously identify the monolayer thickness of the membrane. At least one multilayer island close to the monolayer region has to be resolved, from which quantum oscillations in the electron reflectivity can be observed in order to prove the crystalline order and cleanliness of the membrane. Figure 8(a) displays a LEEM data set taken from a $220 \times 140 \mu\text{m}$ -wide area of a grid with hexagonal holes of $20 \mu\text{m}$ diameter, which has been covered by a well-degassed graphene membrane that was synthesized following the B + CVD growth and the T-B transfer protocol. The displayed image of the membrane has been generated by stitching together 72 LEEM images, each with a $30 \mu\text{m}$ field of view. Every image was acquired at a start voltage energy of 2.5 eV so that contrast reversal indicates a membrane thickness increase/decrease by one atomic layer. Local LEEM I/V data sets acquired at various positions allowed us to identify the local thickness of the freestanding graphene and the red arrows indicate the areas where the membrane consists of mono-, bi-, tri- and four-layer-thick graphene. It is clearly seen that monolayer graphene appears only as a minority phase in the freestanding graphene film, with most of the area consisting of hexagonally shaped few-layer graphene islands with a thickness ranging between two and four atomic layers. In essence, the covered area imaged in figure 8(a) represents a graphene membrane with an average thickness of 2–3 atomic layers. Since after UHV preparation, we never see large areas entirely covered by monolayer graphene, no matter which transfer technique is used to produce CVD-grown freestanding graphene, we conclude that the observed few-layer islands have a stabilizing effect on the graphene film, which is mandatory when wanting to cover large areas on a support grid with ~ 10 – $20 \mu\text{m}$ wide holes.

In fact, when producing stable graphene membranes that are capable of sealing large areas, we intentionally do not remove all carbon from the Cu foil during foil pre-treatment so that the remaining extra carbon can act as a nucleation site for few-layer graphene islands during CVD in agreement with

findings reported in the literature [84]. Thus, although the used CVD growth recipe is identical to the protocol for monolayer graphene growth, the resulting graphene after transfer onto the support grid has rather the properties of the membrane displayed in figure 8(a). This fact partly explains why the CVD growth following the protocol for monolayer graphene may deliver thicker than monolayer graphene films. Nevertheless, having found that freestanding graphene membranes covering large holes seem to be thicker than two atomic layers raises the question of why the successful assembly of freestanding monolayer graphene covering large holes is reported in the literature [47–49]. Although we can only report on our own findings that we did not succeed in producing freestanding monolayer graphene spanning over holes with $>100 \mu\text{m}$ diameter, we may discuss a potential explanation for this discrepancy. Figure 8(b) displays an SEM image reflecting the secondary electron emission yield from an assembled graphene membrane on top of a grid with quadratic holes of $20 \mu\text{m}$ side length. The membrane was synthesized following the B + CVD growth- and T-B transfer protocol. In the top part of figure 8(b), seven holes are imaged where membranes ruptured, while the remaining 42 holes of the imaged area are entirely covered by the graphene film. With the empty holes appearing dark, the graphene-covered holes are easily identified by their homogeneous grayish contrast. In the lower part of the grid, bright lines appear where the membrane is locally folded onto itself, leading to a locally crumpled membrane with about double thickness. Apart from the crumpled areas, the local $20 \times 20 \mu\text{m}$ frames are smoothly covered by the freestanding graphene membrane.

When measuring the Raman spectrum on one of the frames, we obtain sharp G and 2D peaks with the 2D peak height considerably larger than that of the G band (upper spectrum in figure 8(b)). This is the Raman signature of monolayer graphene [107, 108]. When instead searching for another sealed frame of the grid, we see the clear signature of few-layer graphene with a much broader 2D band at a lower peak height than the G peak (the lower Raman spectrum of figure 8(b)) [107, 108]. We suggest that the entire graphene membrane shown in figure 8(b) represents few-layer-thick freestanding graphene and that the monolayer Raman signature results from a turbostratic stacking of the film, which leads to spectral line shapes almost identical to the ones obtained from monolayer graphene [109], similar to the observation of electronically decoupled turbostratic multilayer graphene on SiC [110, 111]. The LEEM images of figure 8(a) support this suggestion. In the upper part of the image, two multilayer islands are marked by red arrows. The flipping contrast relates to subsequent carbon layers with straight step edges indicating the hexagonal shape of the islands. While the left island displays parallel aligned step edges, the step edges of the right island are rotated by about 30° with respect to each other. Knowing that the step edges of CVD-grown graphene on Cu proceed along the zig-zag direction of graphene lattice [112–114] evidences the stacking of aligned or rotated graphene layers in the left and right

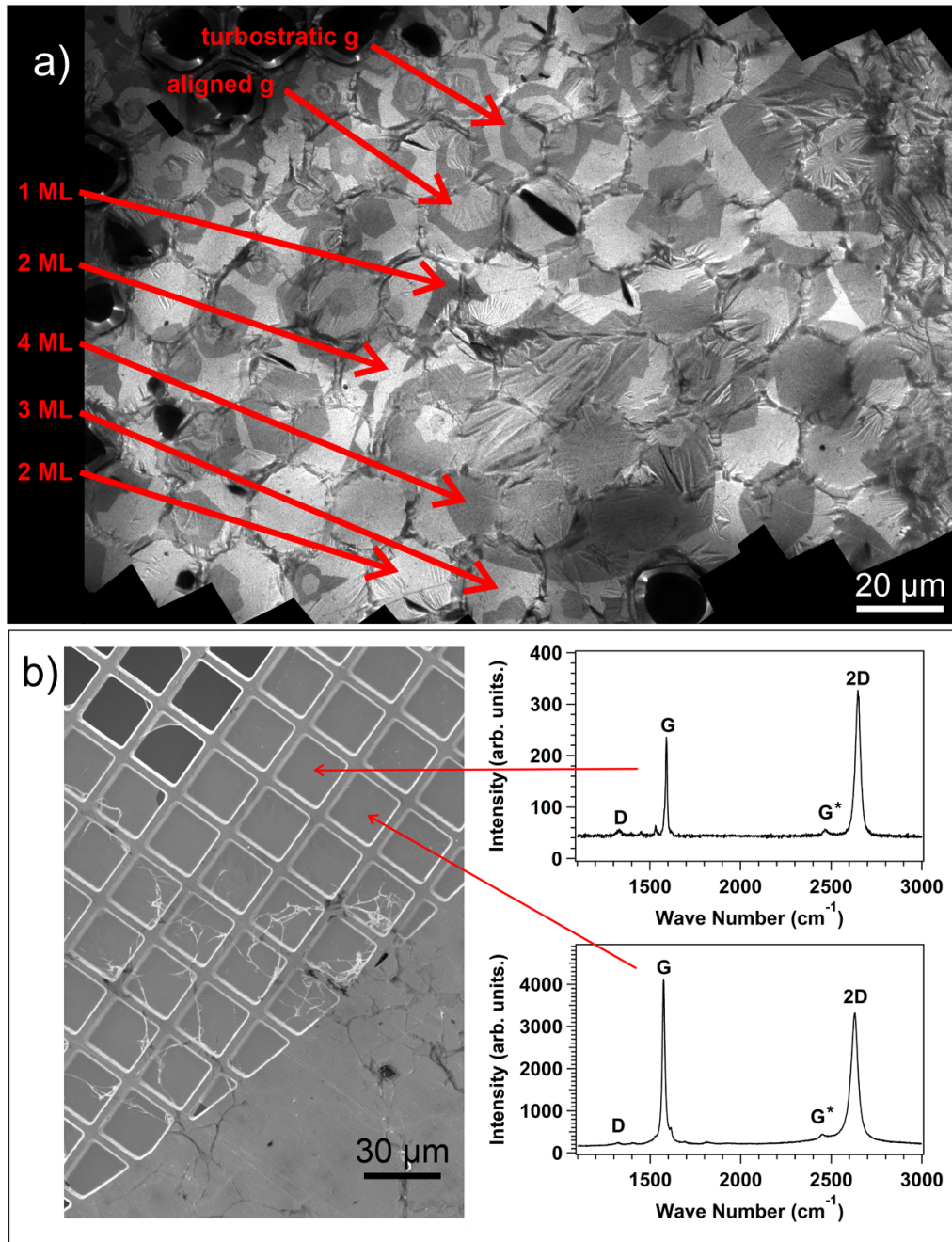


Figure 8. (a) Stitched LEEM images acquired at 2.5 eV with contrast reversal indicating the membrane thickness change by one atomic layer. Local LEEM I/V data allow to assign the local membrane thickness as indicated by arrows. Two few-layer graphene islands are identified in the top part of the image with the stacking of aligned and about 30° rotated layers (see text). (b) SEM image of a grid with quadratic holes of $20\ \mu\text{m}$ side length covered by transferred graphene (primary energy 5 keV). In the left upper edge of the graph, seven membranes are ruptured and appear dark, indicating that the holes with grayish contrast are entirely sealed by graphene. Their homogeneous contrast indicates that no large thickness variations are present in the graphene film. Nevertheless, when locally acquiring Raman data from one of the graphene covered holes, the Raman signature of monolayer graphene is obtained (upper spectrum), while the lower spectrum acquired from another covered hole clearly identifies multilayer graphene. Comparison with the LEEM image in a) leads to the assignment of the monolayer-type Raman spectrum to turbostratic instead of monolayer graphene. This finding questions many reports of monolayer graphene suspended over extended holes (growth and transfer protocol: (a) B + CVD, T-B, (b) B + CVD, T-A; see supplementary material).

multilayer island, respectively. As a result, a Raman spectrum obtained from the left island would lead to the signature of few-layer graphene while the signature of the right island would match the one of monolayer graphene [115]. Thus, we

conclude that locally observing the Raman signature in large suspended graphene films is not sufficient to unequivocally determine the monolayer thickness of freestanding graphene [47, 48].

6.4. LEED spot analysis and flatness of freestanding graphene

Having prepared well-degassed membranes suspended on grids provides the possibility to acquire the LEED patterns of freestanding CVD-grown graphene. Successful preparation is very demanding and requires vacuum annealing at temperatures well above 100 °C for more than 4 h. During this time, enormous degassing of the membrane is observed, leading to a pressure well above 10^{-6} mbar in the UHV system over a time span larger than 1 h. With the typical effective pumping speed of UHV systems ranging between 10 and 100 l s^{-1} , the observed degassing relates to a desorption rate of 2.4×10^{14} particles per second at minimum, or a total desorption of about 1000 monolayer material from a sample area of about 1 cm^2 . Note that this is a lower limit estimation and that the true amount of desorbing material may well be larger by up to two orders of magnitude. After all adsorbates are desorbed, the membranes can be safely annealed to even higher temperatures while maintaining a base pressure in the low 10^{-9} mbar pressure range or even below. As already mentioned, during this degassing treatment in vacuum the membranes have to withstand the mechanical stress induced by the thermal expansion of the supporting frame. This might account for the sorting out of slightly defective membranes; the membrane samples often develop local field emitters after rupturing that make surface analysis using the SPELEEM instrument impossible. Nevertheless, after several years of experience, we were able to obtain good LEED data. Here, we can make use of the finding that the thermal expansion of the supporting grid tends to straighten the freestanding graphene membranes (see figure 6).

Figure 9 shows a data set acquired from freestanding mono- and bilayer graphene acquired at sample temperatures of 60 °C and 300 °C. The CVD-grown graphene membranes were synthesized following the C + CVD growth protocol where the nucleation and growth of few-layer graphene islands was intentionally induced in order to increase the mechanical stability of the resulting membrane. As a result, the synthesized membranes do not host extended areas of freestanding monolayer graphene. Nevertheless, the used SPELEEM microscope at the Nanospectroscopy beamline of Elettra provides the possibility to acquire μ -LEED data from a probe spot of 2 μm diameter [116]. The LEED patterns displayed in figure 9(a) are taken from freestanding monolayer graphene and appear very blurred, which we assign to the varying curvature of the material with respect to the optical axis of the microscope at the sub-micrometer-length scale. This assignment is in agreement with a study performed with the same LEEM apparatus where the vertical corrugation of delaminated freestanding monolayer graphene was evidenced to proceed on the 60 nm lateral wavelength scale [106]. The finding that annealing to 300 °C considerably sharpens the LEED spots supports the picture of a membrane suspended on a drum frame which is strained and flattened by the thermal expansion of the frame at elevated temperature. The upper row of figure 9(a) displays the diffraction patterns acquired at 35 eV at the indicated temperature. Scaling the intensity of both LEED data sets to the (0,0) peak maximum acquired at 25 eV accounts for the peak intensity

reduction at high temperature due to the Debye–Waller factor, and we can visually compare the peak shape changes as a function of annealing. The false color coding of the displayed diffraction patterns demonstrates the sharpening of the (0,0) spot and the first-order diffraction spots at increased sample temperature. In addition, a data set of diffraction patterns was acquired as a function of the irradiating electron beam energy (from 25 to 100 eV in steps of 1 eV), from which the spot profiles along the indicated red line were extracted. Plotting the spot profiles versus the electron energy leads to the graphs displayed below the diffraction patterns. These so-called waterfall plots are similar data sets to the one shown in figure 3(e), but they use a different false color coding for the profile intensity, which is shown on the left side of the graph. Again, the sharpening upon temperature increase is clearly visible, especially for the (0,0) spot profile. The horizontal axis is calibrated to the wave vector k_{\parallel} with 2.95 \AA^{-1} corresponding to the (1,0) spot of the graphene lattice. Using this calibration, we can quantify the (0,0) spot profile by extracting its full width at half maximum (FWHM) from the (0,0) LEED spot taken at 35 eV. Before the temperature increase, the (0,0) spot shows a FWHM of 1.8 \AA^{-1} , which reduces to values ranging between 1.0 \AA^{-1} and 1.3 \AA^{-1} . The slightly asymmetric peak shape is clearly visible and may be attributed to the non-isotropic straining of the membrane induced by the membrane morphology surrounding the probed monolayer graphene area.

Note that in the case of freestanding bilayer graphene, reasonably sharp first-order diffraction peaks appear, and the intensity variations of the diffraction peaks with increasing electron energy are clearly visible in the waterfall plots of figure 9(b). While the observed I/V characteristics of the (0,0) and first-order diffraction spots originate from the constructive/destructive interference of the electron wave reflected from the two stacked carbon layers in bilayer graphene, such effects are absent in freestanding monolayer graphene as can be seen in the waterfall plots of figure 9(a). Thus, in addition to the observed quantum oscillations shown in figure 7, the diffraction data presented in figure 9 also show a clear indication of whether the produced freestanding graphene membranes are made of monolayer graphene. Up to now, we have shown that CVD-grown graphene can be transformed into freestanding graphene from which diffraction data can be acquired. We have also shown that the staircase morphology of CVD-grown graphene on Cu is still imprinted in the membranes after conversion into freestanding graphene, but that intentionally straining the membranes leads to a flattened morphology.

The influence of the membrane morphology on the LEED spot shape is even more pronounced in the second data set acquired from freestanding bilayer graphene, as shown in figure 9(b). Here, asymmetric LEED spots appear in the LEED pattern taken at 60 °C at an electron energy of 35 eV. Again, LEED I/V data sets such as the ones shown for monolayer graphene in figure 9(a) were taken and plotted in a similar way, leading to the diffraction patterns and waterfall plots displayed in figure 9(b). The intensity of each data set has been again scaled to the (0,0) spot maximum intensity acquired at 25 eV and the same false color coding was applied to all displayed graphs. Inspection of the waterfall plot extracted from

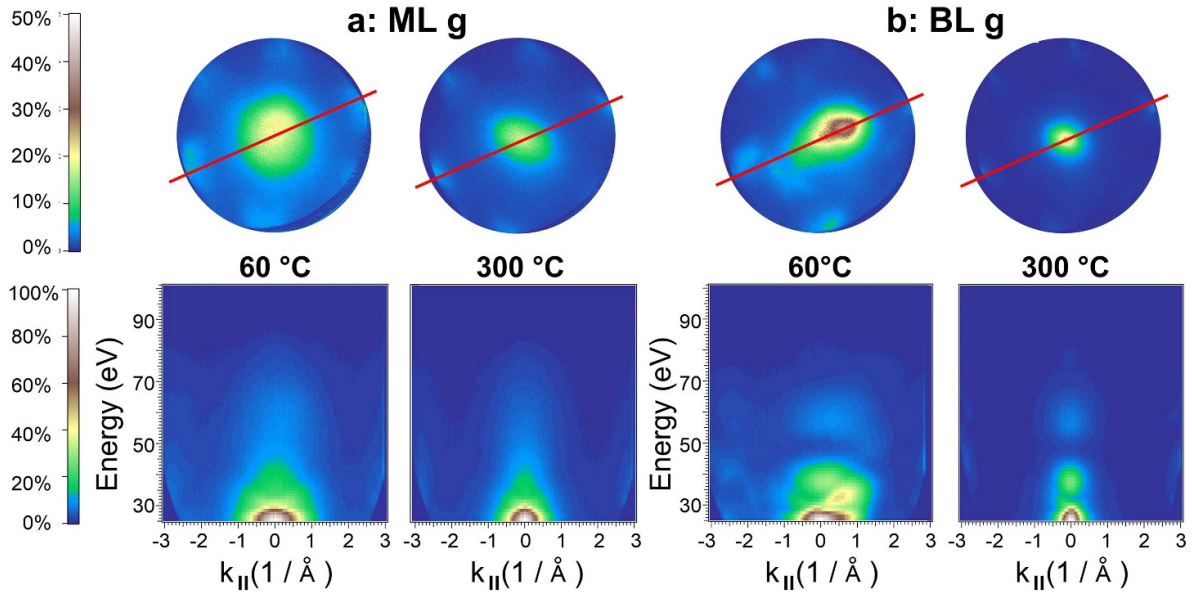


Figure 9. LEED I/V data sets acquired from freestanding mono- and bilayer graphene at 60 °C and 300 °C that has been fixed on a Cu support grid. The LEED patterns were recorded at electron energies increasing from 25 eV up to 100 eV in steps of 1 eV. In the upper row the respective LEED patterns acquired at 35 eV are displayed. Peak intensity profiles were extracted from each data set along the indicated red line and plotted in a waterfall plot with the electron energy as vertical, $k_{||}$ in reciprocal vector units as horizontal axis and the normalized spot intensities color coded according to the displayed false color tables (see text). (a) Diffraction patterns acquired from freestanding monolayer graphene. The (0,0) peak recorded at 35 eV has a FWHM = 1.8 \AA^{-1} at $T = 60 \text{ }^{\circ}\text{C}$ and develops a sharper shape with a FWHM = $(1.0\text{--}1.3) \text{ \AA}^{-1}$ at $T = 300 \text{ }^{\circ}\text{C}$. The sharpening of the (0,0) peak with increasing temperature can also be visually detected in the respective waterfall plots because the peak intensities are scaled and color coded with respect to the same color table. (b) Diffraction patterns acquired from freestanding bilayer graphene. At 60 °C an asymmetric (0,0) peak shape is recorded at an electron energy of 35 eV. The energy dependence of the $k_{||}$ component of the (0,0) spot appears in the waterfall plot and indicates the presence of an inclined plane in addition to the one to which the microscope is aligned. This indicates an imprinted staircase morphology of the local bilayer graphene membrane similar to the case shown for supported graphene in figure 3(e). At the elevated temperature of 300 °C the Cu support grid expands and flattens the bilayer graphene membrane so that a regular hexagonal LEED pattern with much sharper peaks is observed and the (0,0) spot recorded at 35 eV has a FWHM = $(0.5\text{--}0.6) \text{ \AA}^{-1}$. All given k -space values follow the reciprocal space notation including the factor of 2π (growth and transfer protocol: C + CVD, T-B, see supplementary material).

the LEED data taken at 60 °C reveals the presence of a $k_{||}$ component in the (0,0) spot intensity, which accounts for the asymmetric (0,0) peak shape of the displayed diffraction pattern taken at 35 eV. Qualitatively, we can attribute this finding to the presence of an inclined surface plane in addition to the aligned plane of the bilayer graphene membrane. The inclined plane accounts for the diffraction spot dispersion toward the right side with increasing energy. Comparison with the data shown in figure 3(e) proves that also in the freestanding bilayer graphene membrane two differently inclined surface planes are present, although these planes are not as well defined as in the data set taken from the supported graphene. In agreement with the real-space LEEM data displayed in figures 5 and 6, we can conclude that the former morphology of the Cu foil was partly imprinted in the freestanding bilayer graphene, from which the LEED data were extracted. Interestingly, the observed effect of the two differently inclined surface planes on the diffraction data vanishes if the diffraction patterns are acquired from the same bilayer membrane area at the elevated temperature of 300 °C. At this temperature sharp circular diffraction spots are observed. We can conclude that the thermal expansion of the supporting frame strains the membrane and flattens its morphology.

Finally, we discuss the thickness-dependent morphology of freestanding graphene made from CVD-grown g/Cu on membrane areas where the former Cu foil was not faceted and compare it with membranes produced from exfoliated graphene. For this purpose, LEED data were acquired from as flat as possible areas of the CVD-grown graphene membranes, where no indication of the simultaneous presence of inclined facets was observed. Again, graphene membranes were synthesized following the C + CVD growth protocol while intentionally increasing the amount of few-layer graphene islands in the film. Figure 10 displays the room temperature LEED patterns acquired at 40 eV from freestanding mono-, bi-, tri- and four-layer graphene after the membrane thickness was identified by determining the quantum oscillations of the electron reflectivity at low energy. Similar to the data displayed in figure 9, the intensity of each diffraction pattern was scaled to the maximum of the (0,0) spot and the same false color coding was applied, which is shown in the left part of figure 10. One can clearly observe the blurred and asymmetric appearance of the diffraction spots obtained from monolayer graphene, the sharper spots taken from bilayer graphene and the needle-type diffraction peaks acquired from tri- and four-layer graphene. To provide quantitative numbers, the FWHM of the (0,0)

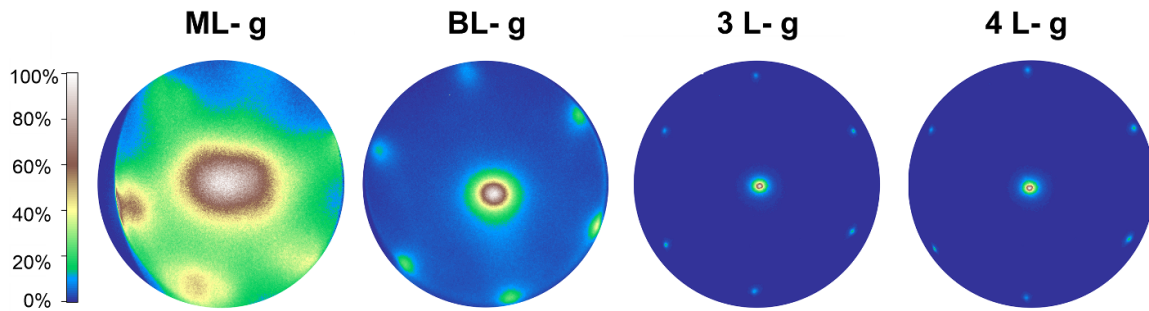


Figure 10. Diffraction patterns acquired at 40 eV from freestanding monolayer (ML), bilayer (BL), three-layer (3-L) and four-layer (4-L) graphene at room temperature with peak shapes of the (0,0) spot leading to the following FWHM values: ML = $(1.5\text{--}2.1) \text{ \AA}^{-1}$, BL = 0.65 \AA^{-1} , 3-L = 0.18 \AA^{-1} , 4-L = 0.18 \AA^{-1} . Note the very diffuse appearance of the monolayer graphene diffraction spots. The displayed diffraction data taken from a flat bilayer graphene membrane lead to much sharper spots. For graphene films with thickness larger than three layers the diffraction data deliver sharp diffraction spots similar to the ones measured from single-crystal surfaces. The applied transfer method may lead to impurities on the membranes and thus, enlarge the broadening of the diffraction peaks. However, this effect can be ruled out to a certain extent (see text). The extracted k -space values follow the reciprocal space notation including the factor of 2π (growth protocol C + CVD, transfer protocol: ML and BL graphene: T-B, 3-L and 4-L graphene: T-C; see supplementary material).

peak was extracted. It ranges between 1.5 and 2.1 \AA^{-1} for monolayer graphene and amounts to 0.65 \AA^{-1} for bilayer graphene in the current data set. Both values are significantly larger than the ones recorded from freestanding exfoliated graphene, which amounted to about 0.8 \AA^{-1} for monolayer and 0.4 \AA^{-1} for bilayer graphene when acquired at the same electron energy with the same instrument [106]. As seen in figure 10, electron diffraction from three- and four-layer-thick CVD-grown freestanding graphene leads to equally sharp spots with a FWHM of the (0,0) beam of 0.18 \AA^{-1} . This number compares to the reported FWHM of the (0,0) diffraction spot of 0.10 \AA^{-1} reported for graphite and to the FWHM of the (0,0) spot derived from supported monolayer g/Cu(111) of the experiment shown in figure 3. The latter amounts to 0.07 \AA^{-1} and matches the reported transfer width of 10 nm of the SPELEEM instrument [106].

The synthesis of CVD-grown freestanding graphene requires contact with wet chemicals when applying the transfer protocol, which is avoided when mechanically exfoliating graphene. Thus, the transfer of CVD-grown graphene might contaminate the membranes, which would explain why the diffraction peaks are about 1.5–2 times broader when compared to the ones acquired from exfoliated graphene [106]. Although we cannot rule out that further optimization of the membrane synthesis route might lead to even sharper diffraction spots, we can confirm that the vertical corrugation of freestanding CVD-grown graphene follows the same trend observed on exfoliated graphene with monolayer graphene being significantly more vertically corrugated than bilayer graphene, which itself is significantly more corrugated than three-layer membranes. The observation that membranes with thicknesses larger or equal to three atomic layers are equally flat fits well with the fact that from three-layer graphene on, a bulk layer exists in the solid, which stabilizes the surface.

When relating the diffraction peak broadening of the (0,0) reflected beam to the vertical corrugation of the graphene membranes we can use equation (6) to estimate the involved

angular variation of the membrane surface normal with respect to the optical axis of the microscope. When doing so, a FWHM of 1.5 \AA^{-1} relates to the nominal variation of $\pm 7^\circ$ for monolayer graphene, while a FWHM of about 0.65 \AA^{-1} for bilayer graphene amounts to $\pm 3^\circ$ and the observed FWHM of 0.18 \AA^{-1} from three- and four-layer graphene relates to an inclination angle variation of $\pm 0.8^\circ$, respectively. The derived numbers do not deviate much from the average value of $\pm 5^\circ$ extracted in a TEM study of suspended exfoliated monolayer graphene [117].

Since one may speculate that the wet chemical treatment might partly account for the broadening of the acquired diffraction peaks, the question arises as to whether or not the chosen transfer protocol influences the quality of the diffraction data. The first two diffraction patterns of mono- and bilayer graphene shown in figure 10 were taken from freestanding graphene synthesized by applying the T-B transfer protocol where the Cu support was chemically dissolved (synthesis route [b] in figure 4). In contrast, the diffraction data acquired from three-layer and four-layer-thick graphene belong to membranes where the CVD-grown graphene was detached from the Cu support following the bubbling transfer protocol T-C (see synthesis route [a] in figure 4). Thus, instead of relating the observed sharpening of the (0,0) diffraction spot to the membrane thickness increase from two to three atomic layers, the effect might be attributed to the potentially superior bubbling transfer protocol used for the synthesis of the three- and four-layer-thick membranes shown in figure 10. However, we consider this explanation as rather unlikely, since we also managed to synthesize freestanding bilayer graphene following the bubbling transfer protocol T-C and obtained a (0,0) diffraction spot FWHM of about 0.6 \AA^{-1} , similar to the shown diffraction data of bilayer graphene synthesized following the Cu dissolution protocol T-B. Freestanding monolayer graphene, suspended over holes large enough to perform μ -LEED measurements, could not be prepared when using the bubbling transfer method and we can use the above argument

only for membranes with thicknesses larger than two atomic layers.

All in all, we can summarize that CVD-grown freestanding graphene may be influenced by the local staircase morphology of the former Cu support foil, but even in areas where the support foil developed a flat geometry, mono- and bilayer graphene membranes do not seem to be flat. Thus, if studies present LEED data of freestanding graphene with sharp diffraction peaks, the generated membranes are most likely made of few-layer graphene [82].

7. Electron transparency of supported and freestanding graphene

After having characterized the morphology, thickness and crystal structure of freestanding CVD-grown graphene, we need to raise the question of what electron transparency of the produced graphene membranes can be obtained. First, the easiest method is to measure the as-grown graphene films, which are still in contact with the support. The samples were grown by following the A + CVD and B + CVD growth protocol, respectively, while pre-treatment and growth were tuned to deliver monolayer graphene. The electron transparency was then measured by creating an electron emission signal underneath the graphene film and determining its attenuation compared to the electron emission from the graphene-free, bare surface. Figures 11(a) and (b) display experiments of this kind. The electron emission from the support can be either generated by photon or by electron irradiation, as was done by our group using XPS or Auger electron spectroscopy (AES) apparatus. The attenuation of the electron emission intensity through the covering layer can be simply derived by measuring the electron emission signal before and after removal of the covering graphene by Ar⁺ sputtering. The measurement strategy is sketched in figure 11(a) and data were successfully acquired from monolayer graphene on Cu in our laboratory in normal electron emission geometry ($\vartheta = 0$) [25]. The performed experiment was difficult as the x-ray gun and the spectrometer had to be switched off during sample sputtering and both devices had to be reliably switched on again to reach identical irradiation and electron detection conditions, which was possible within an error of about 10%. If a spatially resolving spectrometer is available, the experiment can be greatly simplified since one can sputter-clean one side of the sample while the other side is still covered by the CVD-grown graphene layer as sketched in figure 11(b). Data are shown that were acquired with a STAIB Desa 100 Auger spectrometer with an acceptance angle of $\vartheta = 42.3^\circ$, which was turned into a scanning Auger electron microscope by home-built scanning electronics. The data show 100 μm -sized graphene flakes CVD-grown on a Cu foil with half of the sample surface sputter-cleaned in UHV before starting the AES characterization. The image intensity of the Cu(LMM) Auger transition can be used to determine the electron attenuation of the CVD-grown monolayer graphene by comparing the detected Cu(LMM) Auger electron emission yield at 916 eV that originated from areas below the covering graphene flakes with the

one obtained from the uncovered, sputter-cleaned left part of the Cu foil. The contrast in the C(KLL) Auger transition image locates the position of the graphene flakes, which confirms that the graphene-free regions of the non-sputtered right part of the Cu foils appear dark in the Cu(LMM) image. This contrast originates due to the fact that the graphene-free surface is highly oxidized due to the contact with air after transferring the sample from the CVD reactor into the UHV chamber that hosts the AES spectrometer. Since the graphene-covered areas remain oxygen-free, the measured Cu(LMM) signal attenuation of about 65% with respect to the signal of the sputter-cleaned part of the foil exclusively reflects the electron transparency of monolayer graphene for the released electrons at a kinetic energy of 916 eV.

For the electron transparency measurement of freestanding graphene, a similar experiment is performed where the graphene film is transferred onto a grid with quadratic holes of 200 μm side length. The membrane material was synthesized following the B + CDV growth protocol while choosing pre-treatment and growth conditions that led to few-layer graphene growth. In order to provide the maximum cleanliness, a transfer without any PMMA protective layer was used. Figure 11(c) displays optical and secondary electron images of the partly graphene-covered support grid, which confirm that three holes were entirely covered and one hole was half-covered by the transferred graphene membrane. After positioning a clean Ag foil in close vicinity below the grid, the electron emission yield of the Ag(LMM) Auger transition was acquired. The detected electrons had to pass the graphene membranes on their way to the electron analyzer in the line of sight. The electron attenuation is extracted by comparison with the yield of electrons that reached the detector through uncovered parts of the grid. Note that in both experiments of figures 11(b) and (d) the nominal attenuation of the irradiating electron beam at 5 keV does not contribute to the measured signal decrease because the graphene membranes are completely transparent for electrons at this high kinetic energy. The displayed C(KLL) image confirms that the location of the graphene-covered part of the grid is in agreement with the optical and secondary electron image shown in figure 11(c). The contrast of the displayed Ag(LMM) image reflects the signal attenuation of the suspended graphene membrane for the acquired Auger electrons at their kinetic energy of 349 eV, which relates to an electron transparency of 26% at this electron energy.

The derived electron transparency of the supported and freestanding graphene is plotted versus the electron kinetic energy in the top-right panel of figure 11. Xu *et al* performed a similar study on Cu-supported graphene determining the electron transparency by using AES and microscopy [118]. They used a parameter set of the TPP-2M formula for the prediction of the inelastic mean free path of electrons in solid matter [23] in order to compare the experimentally observed and the theoretically expected electron transparency of graphene. The same formula was used by us in order to compare the experimentally observed electron transparency with the theoretically expected values [25]. The solid lines in the electron transparency chart of figure 11 display the predicted electron transmission of monolayer graphene at normal emission ($\vartheta = 0^\circ$)

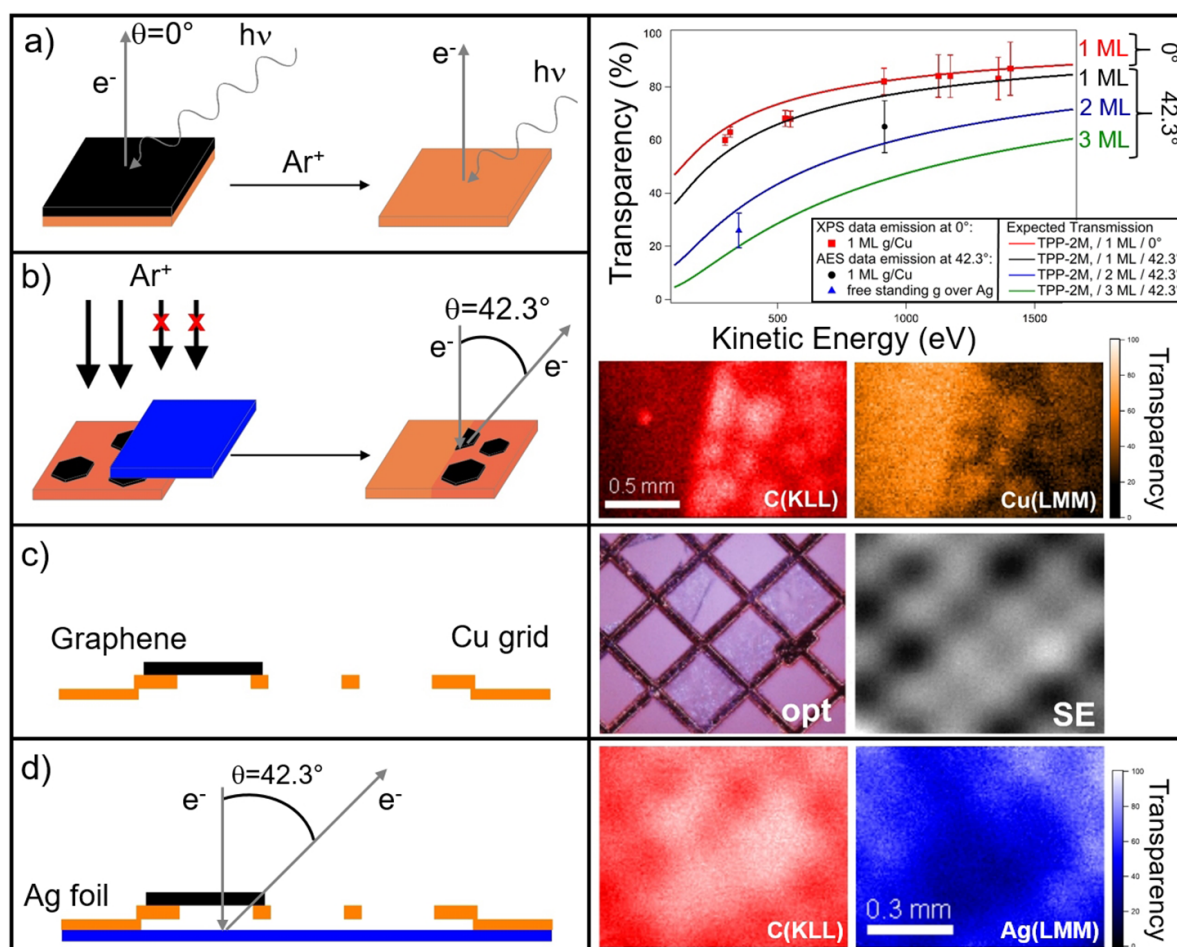


Figure 11. Determining the electron transparency of supported and freestanding graphene. Left column: Sketches of the performed experiments: (a) XPS spectra were acquired before and after removal of the graphene layer. The performed experiments refer to [25]. (b) SAM experiment: the Cu(LMM) signal intensity was acquired from graphene flakes on top of the Cu foil and from the sputter-cleaned Cu foil area close by. (c) Freestanding graphene membranes were transferred onto a support grid with quadratic holes of 200 μm side length. 3.5 holes of the grid were successfully covered as confirmed by optical microscopy and SAM, acquiring the secondary electron emission yield (SE). (d) Placing a silver foil behind the membrane in close vicinity to the grid enabled us to collect the secondary electron emission of the Ag(LMM) transitions. Comparing the emission intensity through empty holes with the one where the electrons have to pass the suspended graphene reflect the electron transparency of the membrane. Right column: Experimental data: optical, SE and SAM images with C(KLL) transition images indicating the positions of the graphene flakes or membranes, respectively. The extracted electron transparencies (see color tables of the Cu(LMM) and Ag(LMM) image) are plotted versus the respective electron kinetic energies in a separate graph where the electron transparencies predicted by the TPP-2M formula using the parameters used by Xu *et al* [118] are also shown as solid lines for the given electron emission geometry ($\vartheta = 0^\circ$ and $\vartheta = 42.3^\circ$) and the nominal graphene layer thickness (growth protocol: (a) A + CVD, (b), (c)+(d) B + CVD, transfer without any PMMA; for details see supplementary material). Reproduced from [25] with permission of The Royal Society of Chemistry.

and of mono-, bi- and trilayer graphene at the emission angle $\vartheta = 42.3^\circ$ accepted by the used AES spectrometer. The red squares indicate the measured values of the XPS experiment sketched in figure 11(a), the black circle indicates the measured attenuation of the g/Cu sample characterized by the AES experiment in figure 11(b), and the blue triangle represents the outcome of the experiment shown in figure 11(d). Comparison with the predicted values indicates that the g/Cu data of the XPS experiment match a monolayer thickness of the supported graphene layer, while the data acquired from g/Cu in the SAM experiment indicate a somewhat larger signal damping through the graphene film matching to a nominal thickness of 1.5 layers. The slightly decreased electron transparency of the CVD-grown graphene might originate from a ‘true’

increase in the effective film thickness, but it may also result from carbonaceous contaminants on top of g/Cu. The latter seems plausible, because the samples of all performed SAM data sets were not annealed. The signal damping measured in the freestanding graphene experiment of figure 11(d) relates to an effective film thickness of between two and three carbon layers, which is qualitatively consistent with the findings discussed with the help of figure 8.

The acquired data show that CVD-grown graphene delivers a membrane material with sufficient electron transparency for applications in environmental XPS to guarantee a high photoelectron signal intensity through the electron window of a graphene-sealed cell. Note that the graphene-based windows shown in figures 6–8 and 11 are orders of magnitude larger

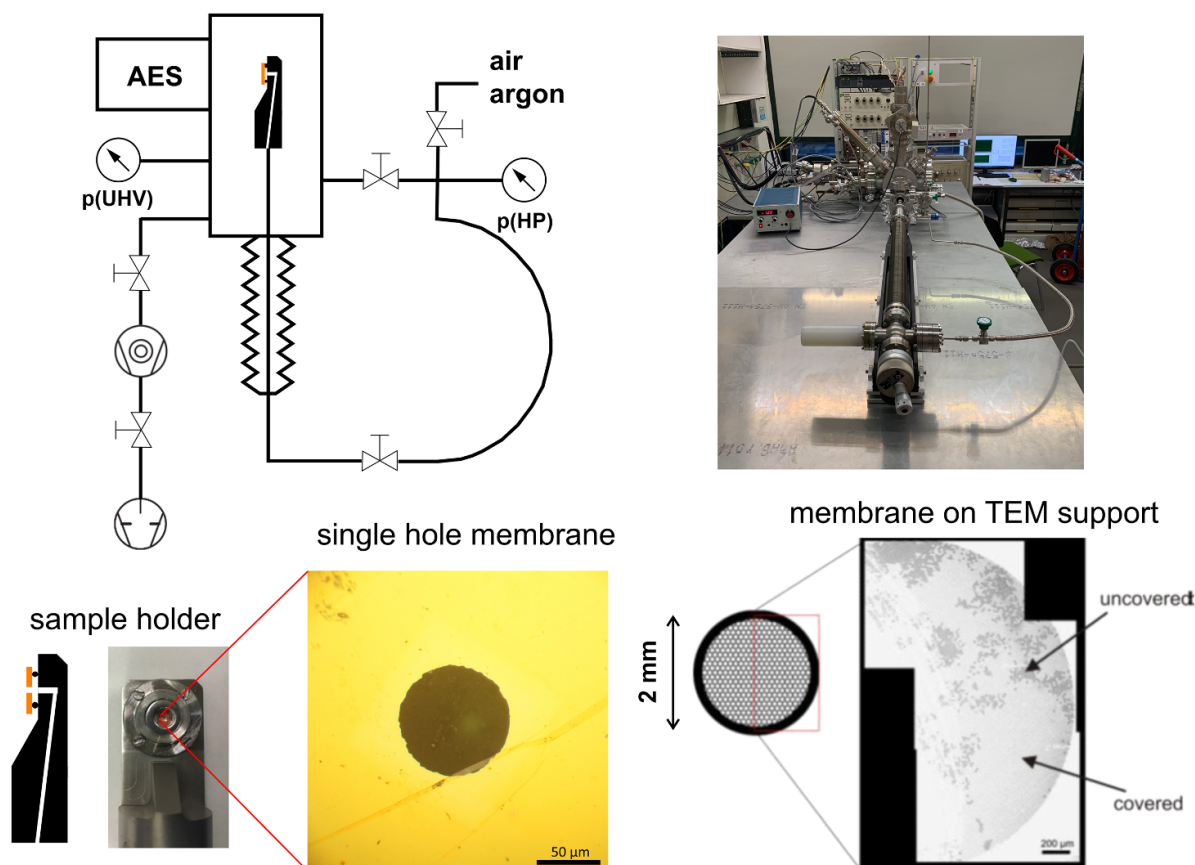


Figure 12. Upper row: laboratory setup to measure the gas leak rate through sealing graphene membranes. A special manipulator allows increasing the pressure $p(\text{HP})$ behind the membrane while measuring the pressure in the main UHV chamber $p(\text{UHV})$. The photograph shows the vacuum chamber relating to the sketch, which also hosts the AES spectrometer used in the experiments of figure 11. Lower row: sketch and photograph of the sample holder and the optical image of a graphene-sealed 100 μm wide single-hole sample as well as stitched SEM images (primary energy 5 keV) showing the right part of a graphene-covered TEM grid of 2 mm diameter with 10 μm -sized holes. Although more than 70% of the TEM grid was covered in graphene, the sealing efficiency does not reach the requirements of an environmental cell experiment. In contrast, environmental cell sealing with a single electron window of 100 μm diameter already meets the required leak tightness (see table 2) (growth protocol: single hole = C + CVD, grid = B + CVD, transfer protocol: T-C).

than the electron windows currently used in ambient pressure XPS experiments following the environmental cell approach. These experiments show the high potential and practical feasibility of the experimental approach, which is why we expect graphene membranes to greatly boost the achievable signal-to-noise ratio for atmospheric pressure PES.

8. Sealing large electron windows by graphene and leak tests

Finally, it remains to be shown that electron windows with diameters in the 10–100 μm range can be sealed leak-tight with the help of transferred, CVD-grown graphene that withstands the forces acting on the membrane sealing during operation at elevated pressure. The upper row of figure 12 displays a sketch and a photograph of the experimental setup built to measure the leakage rate of graphene-sealed electron windows. Note that the UHV chamber also hosts the Auger electron spectrometer, which was used to acquire the data shown in figure 11. In the lower row of figure 12, the sample holder is sketched and photographed. The sample holder has a connection to a

high-pressure gas line. Mounting a leak-tight sample on the sample holder would then seal the high-pressure gas line from the UHV environment of the hosting chamber. The samples may contain either a single hole or an array of holes that have to be closed by a sealing graphene membrane. The optical image shown in figure 12 displays a Si wafer hosting a 50 nm silicon nitride window in which a single hole of 100 μm diameter was etched. The hole was covered by a sealing graphene film which was synthesized along the C + CVD growth protocol while favoring few-layer graphene formation and transferred following the T-C protocol. Alternatively, a graphene sealed array of small holes can be used as the electron window. For preliminary tests, we again used TEM grids where each hole of the grid should be covered by a graphene membrane. The used membrane was synthesized by growing graphene following the B + CVD protocol while again favoring the formation of few-layer graphene and transferred by applying the T-C protocol. The image displayed in the lower right part of figure 12 shows stitched SEM images of the right half of such a grid with 10 μm -sized holes over a vertical distance of 2 mm. Areas appear bright where the holes are entirely covered by

Table 2. Leak tightness and stability test of a circular hole with 100 μm diameter sealed by few-layer graphene.

p (HP) (mbar)	Δp pressure increase (UHV) (mbar)	Leakage rate (mbar \times 1 s ⁻¹)	Equivalent hole diameter (nm)	Fraction of sealed area
10	$<1 \times 10^{-9}$	$<2.75 \times 10^{-8}$	< 130	$>99.9998\%$
80	Membrane rupture	Membrane rupture	Membrane rupture	Membrane rupture

graphene while empty holes or holes with ruptured graphene appear dark. One can see that we managed to cover about 77% of the imaged part of the TEM grid. Although this is already a substantial part of the grid, the coverage does not deliver the sealing efficiency required for high-pressure environmental cell experiments inside a UHV chamber. In contrast, environmental cell experiments with an electron window consisting of a single graphene-sealed hole of 100 μm diameter are already possible, as we show in the last section of this publication.

In order to reliably measure the leakage rate of the membrane, we calibrated the effective pumping speed of the setup, which is pumped by a small 75 l s⁻¹ turbo molecular pump. For this purpose, we inserted an uncovered, 10 μm wide circular aperture and increased the pressure of the high-pressure side to 1 mbar. Under such conditions, we can use the conductance of the aperture of $L = 15.7 \times d^2$ with the aperture diameter given in cm and L given in l s⁻¹ [119] to calculate the effective pumping speed. Measuring the pressure on the UHV side of 5.7×10^{-7} mbar leads to an effective pumping speed of 27.5 ± 1.2 l s⁻¹. Using this number allows us to determine the leakage rate through the graphene-sealed 100 μm diameter hole. The results are tabulated in table 2. When adjusting 10 mbar on the high-pressure side of the cell, no pressure change on the UHV side is measurable, which means that the pressure does not rise by more than 1×10^{-9} mbar. This number represents the precision limit of our measurement chamber with a base pressure in the 10^{-8} mbar range, which results from the fact that a bake-out of the system was not performed in order to avoid any stress on the sealing membrane due to thermal expansion of the support frame. Using these numbers leads to a calculated leak rate below 2.75×10^{-8} mbar \times 1 s⁻¹. This means that the effective size of the leaking hole has a nominal diameter of less than 130 nm and that we managed to seal a fraction of $>99.9998\%$ of the 100 μm diameter hole. Having achieved this sealing quality should enable further XPS experiments at elevated pressure.

Finally, we tested the mechanical stability limit of the graphene-sealed 100 μm diameter hole by gradually increasing the pressure on the high-pressure side up to 80 mbar. Below this value, the sealing remained intact but when exceeding 80 mbar, the membrane broke. The conservative estimation of safe membrane operation conditions discussed in section 3 delivered a pressure limit of about 200 mbar for a 100 μm -sized aperture sealed by monolayer graphene, which means that the order of magnitude is reached in our experiment. Nevertheless, since the used graphene membrane thickness ranges between 2 and 5 carbon layers and the sealing efficiency is poor when covering hole arrays, there is still room for improvement.

9. Summary and outlook

We summarized the work on CVD growth of g/Cu and showed that this synthesis route delivers monolayer graphene with high crystalline quality with respect to both the graphene and the Cu support when using the correct foil pre-treatment procedures. However, freestanding graphene derived from this preparation protocol capable of covering large holes rather represents few-layer graphene. We also showed that the Raman signature of the acquired spectra cannot be used to identify freestanding monolayer graphene, as the Raman signature of turbostratic graphene cannot be easily distinguished from single-layer graphene. We presented novel experiments on how to acquire high-quality LEED data from CVD-grown freestanding graphene. Making use of the μ -LEED technique in a LEEM apparatus, quantum oscillations of (0,0) reflectivity at low kinetic energy were observed and diffraction data were acquired from freestanding mono-, bi-, three- and four-layer graphene. The data indicate that CVD-grown monolayer graphene is considerably and bilayer graphene still slightly vertically corrugated. Graphene membranes with thicknesses larger than or equal to three atomic layers can be considered as having a flat morphology. These findings apply for the local sub- μm length scale. However, the restructuring of the Cu foil during CVD growth induces a mesoscopic morphology change which is imprinted in the CVD-grown graphene film and which remains imprinted even when detaching and transferring the film onto a new support frame. Thermal expansion of the support induces strain in the suspended graphene membrane, which may or may not be a beneficial effect but which should always be taken into account when trying to characterize freestanding CVD-grown graphene. Finally, we could measure the electron transparency and the leak tightness of the generated membrane material. The achieved results are promising and ambient pressure experiments inside environmental cells seem possible even with the use of standard laboratory equipment, which will boost applications and experimental approaches of this novel technique.

Acknowledgments

We thank Dr Simone Dal Zilio and Nicola Cefarin at the Facility of Nano Fabrication FNF@IOM-CNR for producing the Si wafer with the 100 μm hole shown in figure 12, We also thank Professor Joost Winterlin for helpful discussions and Professor Joost Winterlin and Professor Thomas Bein for sharing the laboratory equipment. We also acknowledge financial support from the German Research Foundation (DFG) within the framework of the Priority Program 1459 ‘Graphene’ (GU-521/2-1). This work has partially received

funding from the EU-H2020 research and innovation programme under grant agreement no. 654360 having benefited from the access provided by CNR in Trieste (Italy) within the framework of the NFFA Europe Transnational Access Activity.

ORCID iDs

Paul Leidinger  <https://orcid.org/0000-0003-0662-727X>

Tim Kratky  <https://orcid.org/0000-0002-8402-6640>

Sebastian Günther  <https://orcid.org/0000-0002-2415-232X>

References

- [1] Novoselov K S, Geim A K, Morozov S V, Jiang D, Zhang Y, Dubonos S V, Grigorieva I V and Firsov A A 2004 Electric field effect in atomically thin carbon films *Science* **306** 666–9
- [2] Novoselov K S, Jiang D, Schedin F, Booth T J, Khotkevich V V, Morozov S V and Geim A K 2005 Two-dimensional atomic crystals *Proc. Natl Acad. Sci. USA* **102** 10451–3
- [3] Geim A K and Novoselov K S 2007 The rise of graphene *Nat. Mater.* **6** 183–91
- [4] Castro Neto A H, Guinea F, Peres N M R, Novoselov K S and Geim A K 2009 The electronic properties of graphene *Rev. Mod. Phys.* **81** 109–62
- [5] Lee C, Wei X, Kysar J W and Hone J 2008 Measurement of the elastic properties and intrinsic strength of monolayer graphene *Science* **321** 385–8
- [6] Bunch J S, Verbridge S S, Alden J S, Van Der Zande A M, Parpia J M, Craighead H G and McEuen P L 2008 Impermeable atomic membranes from graphene sheets *Nano Lett.* **8** 2458–62
- [7] Davidovikj D, Scheepers P H, Van Der Zant H S J and Steeneken P G 2017 Static capacitive pressure sensing using a single graphene drum *ACS Appl. Mater. Interfaces* **9** 43205–10
- [8] He Z, Chen W, Liang B, Liu C, Yang L, Lu D, Mo Z, Zhu H, Tang Z and Gui X 2018 Capacitive pressure sensor with high sensitivity and fast response to dynamic interaction based on graphene and porous nylon networks *ACS Appl. Mater. Interfaces* **10** 12816–23
- [9] Schwierz F 2010 Graphene transistors *Nat. Nanotechnol.* **5** 487–96
- [10] Ji K et al 2019 Lithium intercalation into bilayer graphene *Nat. Commun.* **10** 275
- [11] Kuhne M, Paolucci F, Popovic J, Ostrovsky P M, Maier J and Smet J H 2017 Ultrafast lithium diffusion in bilayer graphene *Nat. Nanotechnol.* **12** 895–900
- [12] Ren S, Cui M, Li W, Pu J, Xue Q and Wang L 2018 N-doping of graphene: toward long-term corrosion protection of Cu *J. Mater. Chem. A* **6** 24136–48
- [13] Boretti A, Al-Zubaidy S, Vaclavikova M, Al-Abri M, Castelletto S and Mikhalovsky S 2018 Outlook for graphene-based desalination membranes *npj Clean Water* **1** 5
- [14] Lenard P 1905 Facts (available at: www.nobelprize.org/prizes/physics/1905/lenard/facts/) (Accessed 29 November 2020)
- [15] Parsons D F 1974 Structure of wet specimens in electron microscopy. Improved environmental chambers make it possible to examine wet specimens easily *Science* **186** 407–14
- [16] Butler E P and Hale K F 1981 Dynamic experiments in the electron microscope *Practical Methods in Electron Microscopy* (Amsterdam: North-Holland) vol 9 pp 239–348
- [17] Creemer J F, Helveg S, Hovelting G H, Ullmann S, Molenbroek A M, Sarro P M and Zandbergen H W 2008 Atomic-scale electron microscopy at ambient pressure *Ultramicroscopy* **108** 993–8
- [18] Danilatos G 1991 Review and outline of environmental SEM at present *J. Microsc.* **162** 391–402
- [19] Thiberge S, Nechushtan A, Sprinzak D, Gileadi O, Behar V, Zik O, Chowders Y, Michaeli S, Schlessinger J and Moses E 2004 Scanning electron microscopy of cells and tissues under fully hydrated conditions *Proc. Natl Acad. Sci. USA* **101** 3346–51
- [20] Dai S, Gao W, Zhang S, Graham G W and Pan X 2017 Transmission electron microscopy with atomic resolution under atmospheric pressures *MRS Commun.* **7** 798–812
- [21] 2020 DENS solutions (available at: <https://densolutions.com/>) (Accessed 20 November 2020)
- [22] Powell C J 1974 Attenuation lengths of low-energy electrons in solids *Surf. Sci.* **44** 29–46
- [23] Tanuma S, Shiratori T, Kimura T, Goto K, Ichimura S and Powell C J 2005 Experimental determination of electron inelastic mean free paths in 13 elemental solids in the 50–5000 eV energy range by elastic-peak electron spectroscopy *Surf. Interface Anal.* **37** 833–45
- [24] Kolmakov A, Dikin D A, Cote L J, Huang J, Abyaneh M K, Amati M, Gregoratti L, Guenther S and Kiskinova M 2011 Graphene oxide windows for *in situ* environmental cell photoelectron spectroscopy *Nat. Nanotechnol.* **6** 651–7
- [25] Kraus J, Reichelt R, Guenther S, Gregoratti L, Amati M, Kiskinova M, Yulaev A, Vlasiouk I and Kolmakov A 2014 Photoelectron spectroscopy of wet and gaseous samples through graphene membranes *Nanoscale* **6** 14394–403
- [26] Joyner R W, Roberts M W and Yates K 1979 A “high-pressure” electron spectrometer for surface studies *Surf. Sci.* **87** 501–9
- [27] Pantförder J, Pöllmann S, Zhu J, Borgmann D, Denecke R and Steinrück H-P 2005 New setup for *in situ* x-ray photoelectron spectroscopy from ultrahigh vacuum to 1 mbar *Rev. Sci. Instrum.* **76** 014102
- [28] Eriksson S K et al 2014 A versatile photoelectron spectrometer for pressures up to 30 mbar *Rev. Sci. Instrum.* **85** 075119
- [29] Ogletree D F, Bluhm H, Lebedev G, Fadley C S, Hussain Z and Salmeron M 2002 A differentially pumped electrostatic lens system for photoemission studies in the millibar range *Rev. Sci. Instrum.* **73** 3872–7
- [30] Bluhm H et al 2006 Soft X-ray microscopy and spectroscopy at the molecular environmental science beamline at the advanced light source *J. Electron Spectrosc. Relat. Phenom.* **150** 86–104
- [31] Salmeron M and Schlogl R 2008 Ambient pressure photoelectron spectroscopy: a new tool for surface science and nanotechnology *Surf. Sci. Rep.* **63** 169–99
- [32] Schnadt J et al 2012 The new ambient-pressure X-ray photoelectron spectroscopy instrument at MAX-lab *J. Synchrotron Radiat.* **19** 701–4
- [33] Amann P et al 2019 A high-pressure x-ray photoelectron spectroscopy instrument for studies of industrially relevant catalytic reactions at pressures of several bars *Rev. Sci. Instrum.* **90** 103102
- [34] Velasco-Vélez J J et al 2015 Photoelectron spectroscopy at the graphene-liquid interface reveals the electronic structure of an electrodeposited cobalt/graphene electrocatalyst *Angew. Chem., Int. Ed.* **54** 14554–8
- [35] Velasco-Vélez J J et al 2016 Atmospheric pressure X-ray photoelectron spectroscopy apparatus: bridging the pressure gap *Rev. Sci. Instrum.* **87** 053121

- [36] Yulaev A, Guo H, Strelcov E, Chen L, Vlasiouk I and Kolmakov A 2017 Graphene microcapsule arrays for combinatorial electron microscopy and spectroscopy in liquids *ACS Appl. Mater. Interfaces* **9** 26492–502
- [37] Guo H, Strelcov E, Yulaev A, Wang J, Appathurai N, Urquhart S, Vinson J, Sahu S, Zwolak M and Kolmakov A 2017 Enabling photoemission electron microscopy in liquids via graphene-capped microchannel arrays *Nano Lett.* **17** 1034–41
- [38] Jincan Z *et al* 2017 Clean transfer of large graphene single crystals for high-intactness suspended membranes and liquid cells *Adv. Mater.* **29** 1700639
- [39] Yuk J M, Park J, Ercius P, Kim K, Hellebusch D J, Crommie M F, Lee J Y, Zettl A and Alivisatos A P 2012 High-resolution EM of colloidal nanocrystal growth using graphene liquid cells *Science* **336** 61–4
- [40] Krueger M, Berg S, Stone D A, Strelcov E, Dikin D A, Kim J, Cote L J, Huang J and Kolmakov A 2011 Drop-casted self-assembling graphene oxide membranes for scanning electron microscopy on wet and dense gaseous samples *ACS Nano* **5** 10047–54
- [41] Kolmakov A, Gregoratti L, Kiskinova M and Günther S 2016 Recent approaches for bridging the pressure gap in photoelectron microspectroscopy *Top. Catal.* **59** 448–68
- [42] Kolmakov A *et al* 2018 Graphene windows enable photoelectron microscopies of liquid samples *Microsc. Microanal.* **24** 64–7
- [43] Wu C H, Weatherup R S and Salmeron M B 2015 Probing electrode/electrolyte interfaces *in situ* by x-ray spectroscopies: old methods, new tricks *Phys. Chem. Chem. Phys.* **17** 30229–39
- [44] Weatherup R S, Eren B, Hao Y, Bluhm H and Salmeron M B 2016 Graphene membranes for atmospheric pressure photoelectron spectroscopy *J. Phys. Chem. Lett.* **7** 1622–7
- [45] Weatherup R S, Wu C H, Escudero C, Pérez-Dieste V and Salmeron M B 2018 Environment-dependent radiation damage in atmospheric pressure x-ray spectroscopy *J. Phys. Chem. B* **122** 737–44
- [46] Mom R, Frevel L, Velasco-Vélez -J-J, Plodinec M, Knop-Gericke A and Schlögl R 2019 The oxidation of platinum under wet conditions observed by electrochemical x-ray photoelectron spectroscopy *J. Am. Chem. Soc.* **141** 6537–44
- [47] Lee C-K *et al* 2014 Monatomic chemical-vapor-deposited graphene membranes bridge a half-millimeter-scale gap *ACS Nano* **8** 2336–44
- [48] Chen Y M, He S M, Huang C H, Huang C C, Shih W P, Chu C L, Kong J, Li J and Su C Y 2016 Ultra-large suspended graphene as a highly elastic membrane for capacitive pressure sensors *Nanoscale* **8** 3555–64
- [49] Afyouni Akbari S, Ghafarinia V, Larsen T, Parmar M M and Villanueva L G 2020 Large suspended monolayer and bilayer graphene membranes with diameter up to 750 μm *Sci. Rep.* **10** 6426
- [50] Khasanah N, Bolouki N, Huang T-Y, Hong Y-Z, Chung W-L, Woon W-Y, Su C-Y and Kuramitsu Y 2017 Large-area suspended graphene as a laser target to produce an energetic ion beam *High Power Laser Sci. Eng.* **5** e18
- [51] Hu H *et al* 2017 Large-scale suspended graphene used as a transparent substrate for infrared spectroscopy *Small* **13** 1603812
- [52] Shin Y, Lozada-Hidalgo M, Sambricio J L, Grigorieva I V, Geim A K and Casiraghi C 2016 Raman spectroscopy of highly pressurized graphene membranes *Appl. Phys. Lett.* **108** 221907
- [53] Wang L, Williams C M, Boutilier M S H, Kidambi P R and Karnik R 2017 Single-layer graphene membranes withstand ultrahigh applied pressure *Nano Lett.* **17** 3081–8
- [54] Cui T, Mukherjee S, Sudeep P M, Colas G, Najafi F, Tam J, Ajayan P M, Singh C V, Sun Y and Filleter T 2020 Fatigue of graphene *Nat. Mater.* **19** 405–11
- [55] Locatelli A, Aballe L, Mentès T O, Kiskinova M and Bauer E 2006 Photoemission electron microscopy with chemical sensitivity: SPELEEM methods and applications *Surf. Interface Anal.* **38** 1554–7
- [56] Mentès T O, Zamborlini G, Sala A and Locatelli A 2014 Cathode lens spectromicroscopy: methodology and applications *Beilstein J. Nanotechnol.* **5** 1873–86
- [57] Kraus J, Boecklein S, Reichelt R, Guenther S, Santos B, Mentès T O and Locatelli A 2013 Towards the perfect graphene membrane?—Improvement and limits during formation of high quality graphene grown on Cu-foils *Carbon* **64** 377–90
- [58] Kraus J, Böbel M and Günther S 2016 Suppressing graphene nucleation during CVD on polycrystalline Cu by controlling the carbon content of the support foils *Carbon* **96** 153–65
- [59] ScientaOmicron 2020 XM1000 (available at: <https://scientaomicron.com/en/Components/photon-sources/XM-1000>) (Accessed 29 November 2020)
- [60] SPECS Focus 500/600 (available at: www.specs-group.com/nc/specs/products/detail/focus-500600/) (Accessed 20 November 2020)
- [61] Mangolini F, Åhlund J, Wabiszewski G E, Adiga V P, Egberts P, Steller F, Backlund K, Karlsson P G, Wannberg B and Carpick R W 2012 Angle-resolved environmental x-ray photoelectron spectroscopy: a new laboratory setup for photoemission studies at pressures up to 0.4 torr *Rev. Sci. Instrum.* **83** 093112
- [62] Günther S, Kaulich B, Gregoratti L and Kiskinova M 2002 Photoelectron microscopy and applications in surface and materials science *Prog. Surf. Sci.* **70** 187–260
- [63] Briscoe B J and Panesar S S 1991 The application of the blister test to an elastomeric adhesive *Proc. Math. Phys. Sci.* **433** 23–43
- [64] Wan K-T and Mai Y-W 1995 Fracture mechanics of a new blister test with stable crack growth *Acta Metall. Mater.* **43** 4109–15
- [65] Koenig S P, Boddeti N G, Dunn M L and Bunch J S 2011 Ultrastrong adhesion of graphene membranes *Nat Nano* **6** 543–6
- [66] Liu F, Ming P and Li J 2007 *Ab initio* calculation of ideal strength and phonon instability of graphene under tension *Phys. Rev. B* **76** 064120
- [67] Al-Jishi R and Dresselhaus G 1982 Lattice-dynamical model for graphite *Phys. Rev. B* **26** 4514–22
- [68] Li X, Cai W, Colombo L and Ruoff R S 2009 Evolution of graphene growth on Ni and Cu by carbon isotope labeling *Nano Lett.* **9** 4268–72
- [69] Huang P Y *et al* 2011 Grains and grain boundaries in single-layer graphene atomic patchwork quilts *Nature* **469** 389–92
- [70] Ruiz-Vargas C S, Zhuang H L, Huang P Y, Van Der Zande A M, Garg S, McEuen P L, Muller D A, Hennig R G and Park J 2011 Softened elastic response and unzipping in chemical vapor deposition graphene membranes *Nano Lett.* **11** 2259–63
- [71] Li X *et al* 2009 Large-area synthesis of high-quality and uniform graphene films on copper foils *Science* **324** 1312–4
- [72] Rasool H I, Song E B, Allen M J, Wassei J K, Kaner R B, Wang K L, Weiller B H and Gimzewski J K 2010 Continuity of graphene on polycrystalline copper *Nano Lett.* **11** 251–6
- [73] Nie S, Wu W, Xing S, Yu Q, Bao J, Pei -S-S and McCarty K F 2012 Growth from below: bilayer graphene on copper by chemical vapor deposition *New J. Phys.* **14** 093028

- [74] Nguyen V L *et al* 2015 Seamless stitching of graphene domains on polished copper (111) foil *Adv. Mater.* **27** 1376–82
- [75] Brown L *et al* 2014 Polycrystalline graphene with single crystalline electronic structure *Nano Lett.* **14** 5706–11
- [76] Wang H, Wang G, Bao P, Yang S, Zhu W, Xie X and Zhang W-J 2012 Controllable synthesis of submillimeter single-crystal monolayer graphene domains on copper foils by suppressing nucleation *J. Am. Chem. Soc.* **134** 3627–30
- [77] Yan Z, Lin J, Peng Z, Sun Z, Zhu Y, Li L, Xiang C, Samuel E L, Kittrell C and Tour J M 2012 Toward the synthesis of wafer-scale single-crystal graphene on copper foils *ACS Nano* **6** 9110–7
- [78] Ya-Ping H, Yi-Hung C, He-Guang T and Mario H 2016 Reducing the graphene grain density in three steps *Nanotechnology* **27** 105602
- [79] Hao Y F *et al* 2013 The role of surface oxygen in the growth of large single-crystal graphene on copper *Science* **342** 720–3
- [80] Gan L and Luo Z 2013 Turning off hydrogen to realize seeded growth of subcentimeter single-crystal graphene grains on copper *ACS Nano* **7** 9480–8
- [81] Eres G, Regmi M, Rouleau C M, Chen J, Ivanov I N, Puzos A A and Geoghegan D B 2014 Cooperative island growth of large-area single-crystal graphene on copper using chemical vapor deposition *ACS Nano* **8** 5657–69
- [82] Xu X *et al* 2016 Ultrafast growth of single-crystal graphene assisted by a continuous oxygen supply *Nat Nano* **11** 930–5
- [83] Braeuninger-Weimer P, Brennan B, Pollard A J and Hofmann S 2016 Understanding and controlling Cu-catalyzed graphene nucleation: the role of impurities, roughness, and oxygen scavenging *Chem. Mater.* **28** 8905–15
- [84] Luo D *et al* 2019 Adlayer-free large-area single crystal graphene grown on a Cu(111) foil *Adv. Mater.* **31** e1903615
- [85] Reckinger N, Tang X, Joucken F, Lajaunie L, Arenal R, Dubois E, Hackens B, Henrard L and Colomer J-F 2016 Oxidation-assisted graphene heteroepitaxy on copper foil *Nanoscale* **8** 18751–9
- [86] Jin S *et al* 2018 Colossal grain growth yields single-crystal metal foils by contact-free annealing *Science* **362** 1021–5
- [87] Srivastava N, Gao Q, Widom M, Feenstra R M, Nie S, McCarty K F and Vlasiouk I V 2013 Low-energy electron reflectivity of graphene on copper and other substrates *Phys. Rev. B* **87** 245414
- [88] Zeller P, Ma X and Günther S 2017 Indexing moiré patterns of metal-supported graphene and related systems: strategies and pitfalls *New J. Phys.* **19** 013015
- [89] Tang W X, Man K L, Huang H C, Woo C H and Altman M S 2002 Growth shapes of Ag crystallites on the Si(111) surface *J. Vac. Sci. Technol. B* **20** 2492–5
- [90] Wang Y, Zheng Y, Xu X, Dubuisson E, Bao Q, Lu J and Loh K P 2011 Electrochemical delamination of CVD-grown graphene film: toward the recyclable use of copper catalyst *ACS Nano* **5** 9927–33
- [91] Gao L *et al* 2012 Repeated growth and bubbling transfer of graphene with millimetre-size single-crystal grains using platinum *Nat. Commun.* **3** 699
- [92] Lin Y C, Jin C, Lee J C, Jen S F, Suenaga K and Chiu P W 2011 Clean transfer of graphene for isolation and suspension *ACS Nano* **5** 2362–8
- [93] Yulaev A, Cheng G, Hight Walker A R, Vlasiouk I V, Myers A, Leite M S and Kolmakov A 2016 Toward clean suspended CVD graphene *RSC Adv.* **6** 83954–62
- [94] Matruglio A, Nappini S, Naumenko D, Magnano E, Bondino F, Lazzarino M and Dal Zilio S 2016 Contamination-free suspended graphene structures by a Ti-based transfer method *Carbon* **103** 305–10
- [95] Kim S J *et al* 2015 Ultraclean patterned transfer of single-layer graphene by recyclable pressure sensitive adhesive films *Nano Lett.* **15** 3236–40
- [96] Leong W S *et al* 2019 Paraffin-enabled graphene transfer *Nat. Commun.* **10** 867
- [97] Suk J W, Kitt A, Magnuson C W, Hao Y, Ahmed S, An J, Swan A K, Goldberg B B and Ruoff R S 2011 Transfer of CVD-grown monolayer graphene onto arbitrary substrates *ACS Nano* **5** 6916–24
- [98] Weatherup R S 2018 2D material membranes for operando atmospheric pressure photoelectron spectroscopy *Top. Catal.* **61** 2085–102
- [99] Regan W, Alem N, Alemán B, Geng B, Girit Ç, Maserati L, Wang F, Crommie M and Zettl A 2010 A direct transfer of layer-area graphene *Appl. Phys. Lett.* **96** 113102
- [100] Liu W, Li H, Xu C, Khatami Y and Banerjee K 2011 Synthesis of high-quality monolayer and bilayer graphene on copper using chemical vapor deposition *Carbon* **49** 4122–30
- [101] Aleman B *et al* 2010 Transfer-free batch fabrication of large-area suspended graphene membranes *ACS Nano* **4** 4762–8
- [102] Algara-Siller G, Lehtinen O, Turchanin A and Kaiser U 2014 Dry-cleaning of graphene *Appl. Phys. Lett.* **104** 153115
- [103] Zande A M V D, Barton R A, Alden J S, Ruiz-Vargas C S, Whitney W S, Pham P H Q, Park J, Parpia J M, Craighead H G and McEuen P L 2010 Large-scale arrays of single-layer graphene resonators *Nano Lett.* **10** 4869–73
- [104] Zakharchenko K V, Katsnelson M I and Fasolino A 2009 Finite temperature lattice properties of graphene beyond the quasiharmonic approximation *Phys. Rev. Lett.* **102** 046808
- [105] Lide D R (ed) 2008 *CRC Handbook of Chemistry and Physics* 88th edn (Boca Raton, FL: CRC Press, Taylor & Francis Group)
- [106] Locatelli A, Knox K R, Cvetko D, Mentese T O, Niño M A, Wang S, Yilmaz M B, Kim P, Osgood R M and Morgante A 2010 Corrugation in exfoliated graphene: an electron microscopy and diffraction study *ACS Nano* **4** 4879–89
- [107] Malard L M, Pimenta M A, Dresselhaus G and Dresselhaus M S 2009 Raman spectroscopy in graphene *Phys. Rep.* **473** 51–87
- [108] Malard L M, Mafra D L, Doorn S K and Pimenta M A 2009 Resonance Raman scattering in graphene: probing phonons and electrons *Solid State Commun.* **149** 1136–9
- [109] Fang W *et al* 2013 Rapid identification of stacking orientation in isotopically labeled chemical-vapor grown bilayer graphene by Raman spectroscopy *Nano Lett.* **13** 1541–8
- [110] Hass J, Varchon F, Millán-Otoya J E, Sprinkle M, Sharma N, De Heer W A, Berger C, First P N, Magaud L and Conrad E H 2008 Why multilayer graphene on 4H–SiC (000 1) behaves like a single sheet of graphene *Phys. Rev. Lett.* **100** 125504
- [111] Pradeepkumar A, Gaskill D K and Iacopi F 2020 Electronic and transport properties of epitaxial graphene on SiC and 3C–SiC/Si: a review *Appl. Sci.* **10** 4350
- [112] Krauss B, Nemes-Incze P T, Skakalova V, Biro L S P, Klitzing K V and Smet J H 2010 Raman scattering at pure graphene zigzag edges *Nano Lett.* **10** 4544–8
- [113] Yu Q *et al* 2011 Control and characterization of individual grains and grain boundaries in graphene grown by chemical vapour deposition *Nat. Mater.* **10** 443–9
- [114] Shu H, Chen X, Tao X and Ding F 2012 Edge structural stability and kinetics of graphene chemical vapor deposition growth *ACS Nano* **6** 3243–50

- [115] Kim K, Coh S, Tan L Z, Regan W, Yuk J M, Chatterjee E, Crommie M F, Cohen M L, Louie S G and Zettl A 2012 Raman spectroscopy study of rotated double-layer graphene: misorientation-angle dependence of electronic structure *Phys. Rev. Lett.* **108** 246103
- [116] Reichelt R, Günther S, Winterlin J, Moritz W, Aballe L and Montes T O 2007 Low energy electron diffraction and low energy electron microscopy microspot I/V analysis of the (4x4)O structure on Ag(111)O: surface oxide or reconstruction? *J. Chem. Phys.* **127** 134706
- [117] Meyer J C, Geim A K, Katsnelson M I, Novoselov K S, Booth T J and Roth S 2007 The structure of suspended graphene sheets *Nature* **446** 60–3
- [118] Xu M, Fujita D, Gao J and Hanagata N 2010 Auger electron spectroscopy: a rational method for determining thickness of graphene films *ACS Nano* **4** 2937–45
- [119] Wutz M, Adam H and Walcher W 1992 *Theorie Und Praxis Der Vakuumtechnik* (Leipzig: Teubner) 1 Online-Ressource (696S)